CHAPTER IV

EXPERIMENTAL RESULTS AND DISCUSSIONS

The experimental results on the growth of self-assembled InP ring-shape quantum dot molecules (QDMs) in the $In_{0.5}Ga_{0.5}P$ matrices on GaAs (001) substrate are reported and discussed in this chapter. The growth conditions of $In_{0.5}Ga_{0.5}P$ layer including the deposition rate and the In composition are calibrated via scanning electron microscopy and high resolution x-ray diffraction measurement. By using reflection high energy diffraction observation, the InP ring-shape QDM formation can be *in situ* monitored. The possible formation mechanism of the InP ring-shape QDMs is presented. The fundamental parameters of the growth process are systematically examined to provide the understanding of the InP ring-shape QDM formation and the adjusting of InP ring-shape QDM properties by changing growth parameters. The effects of deposition temperature, In thickness, In deposition rates, and crystallization temperature on the QDM array have been studied by using atomic force microscopy and photoluminescence measurements. Finally, transmission electron microscopy has been utilized for investigating the cross-section of InP ring-shape QDM structure.

4.1 Characterization of $In_{0.5}Ga_{0.5}P$ layer on GaAs Substrate.

According to Kurtenbach et al. (1995); (1996); Zundel et al. (1998), the appropriate substrate temperature, phosphorous (P_2) flux intensity or beam equivalent pressure (BEP) and growth rate for the growth of InGaP layer which has lattice-matched with GaAs substrate by solid-source molecular beam epitaxy using GaP decomposition source are 470 °C, 5×10^{-6} Torr and 1 ML/s, respectively. Yoon et al. (2000) proposed that, with increasing of the P_2 BEP or BEP of V/III ratio, not only the energy band gap of this layer will shifts towards higher energy, but also the full-width at half-maximum (FWHM) of a photoluminescence (PL) peak becomes narrower, and the luminescence intensity becomes higher. Unfortunately, in this work, high P_2 BEP could not use because of the limitation of the pump system. Therefore, the growth conditions of InGaP layer has been adjusted using substrate temperature, high P_2 BEP and growth rate of 470 °C, 2×10^{-6} Torr and 0.5 ML/s, respectively. Due to the decreasing of P_2 BEP, the growth rate had to

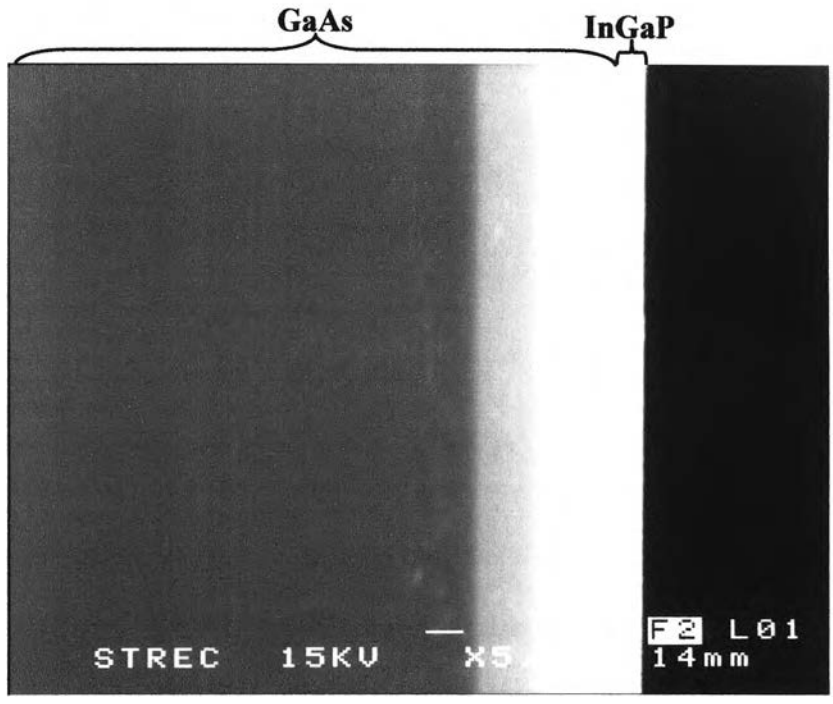

Figure 4.1 The SEM image of 1-μm-thick InGaP layer grown on GaAs (001) substrate.

be reduced corresponding to the layer formation time in order to preserve the good crystal quality. As a result, although theP_2 BEP was limited, the layer surfaces were still smooth and insignificantly changed with P_2 BEP (Yoon et al., 2000).

Since the growth rate of InGaP layer was indirectly calibrated by equivalent to that of InGaAs as explained in chapter 3, the scanning electron microscopy (SEM) has been utilized to examine the thickness of InGaP layer and confirm the real growth rate. SEM image in figure 4.1 reveals that 1-μm-thickness of InGaP layer was grown using the deposition time of 2 hours. The acquired growth rate was 0.5 ML/s corresponding to the In and Ga flux intensities from the growth rate calibration in chapter 3. As a result, this method was employed for calibrating the growth rate of InGaP layer in this work.

Not only the growth rate but also the crystal quality and In composition of InGaP layer that should be considered. The high resolution x-ray diffraction (HRXRD) measurement has been carried out to study the lattice matching between InGaP layer and GaAs substrate. The wavelength of x-ray beam used in this work is 1.540598 Å and the lattice constant of InGaP is desired equivalent to that of GaAs (5.65325 Å). The XRD (004) 2θ-ω pattern of InGaP/GaAs is shown in figure 4.2. There exist two distinct peaks in this spectrum. The higher peak corresponds to the GaAs layer and lower one

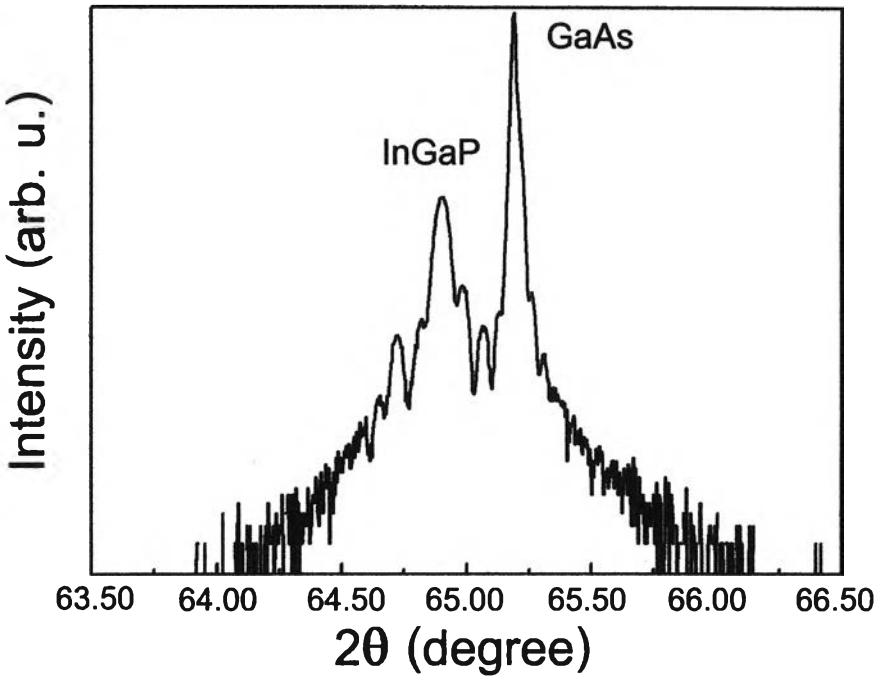

Figure 4.2 The XRD spectrum of 200 nm InGaP layer grown on GaAs (001) substrate in (004).

corresponds to the InGaP layer. Clear Pendellösung fringes (thickness fringe peaks) are observed. This implies that the alloy composition is homogeneous and the layer has high structural quality. Calculated via the X' Pert epitaxy program (HRXRD analysis program), the lattice constant of InGaP is 5.67517 Å, lattice mismatch between InGaP and GaAs is 0.39 %, In composition is 0.54 and the compressive stain is 0.19 %. These values are estimated by assuming that the in-plane lattice constant ($a_{//}$) of InGaP and GaAs are equal.

In order to confirm the In composition, the room temperature (300 K) micro-PL was performed and the optical properties of InGaP layer has been investigated. The PL spectrum of 200-nm-thick InGaP layer grown on GaAs (001) substrate is shown in figure 4.3. In accordance with Moon et al. (1974), the lattice constant of $Ga_y\ In_{1-y}\ As_x\ P_{1-x}$ ($a_{Ga_yIn_{1-y}As_xP_{1-x}}$) and the energy gap of $Ga_y\ In_{1-y}\ As_x\ P_{1-x}$ ($E_{g(Ga_yIn_{1-y}As_xP_{1-x})}$) at 300 K can determine by

$$a_{Ga_yIn_{1-y}As_xP_{1-x}} = 5.8687 + 0.1896x - 0.4175y + 0.0124xy \qquad (4.1)$$

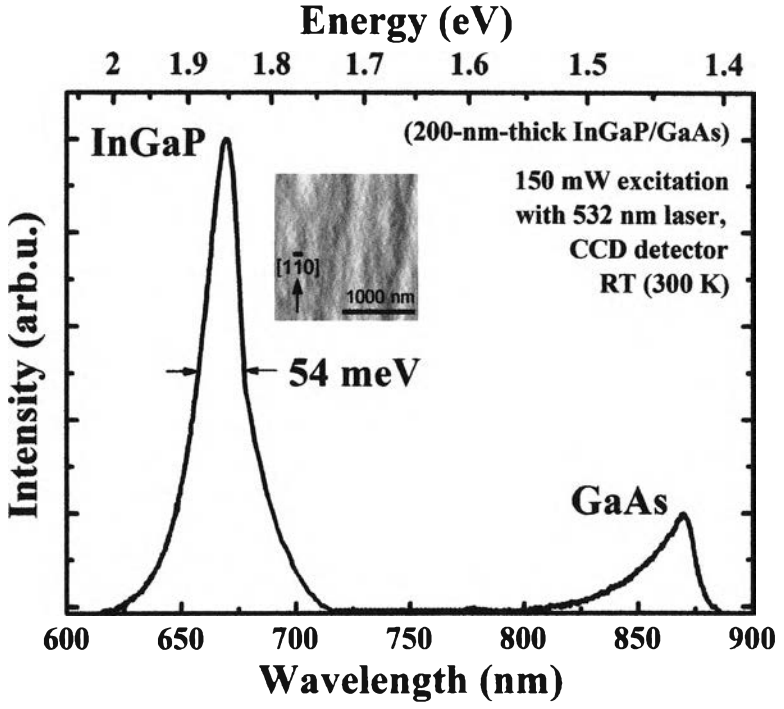

Figure 4.3 The room temperature (300 K) PL spectrum of 200-nm-thick InGaP layer grown on GaAs (001) substrate.

$$E_{g(Ga_yIn_{1-y}As_xP_{1-x})} = 1.35 - x + 1.4y - 0.33xy - (0.758 - 0.28x)y(1-y) - (0.101 + 0.109y)x(1-x) \quad (4.2)$$

The PL spectrum in figure 4.3 has two emission peaks. The highest peak at 1.86 eV with FWHM of 54 meV related to the energy gap of InGaP layer and the lower one at 1.42 eV belongs to GaAs bulk. The sharp lnGaP peak reveals good crystal quality of InGaP layer. From the equation (4.1), (4.2) and (2.11), the calculated In composition of InGaP, lattice constant of InGaP and lattice mismatch between InGaP and GaAs are 0.5, 5.66 Å and 0.18 %, respectively. This In composition is more precise than that from HRXRD calculation because it is directly verified from the energy gap of InGaP layer and the obtained lattice constant is the total lattice constant. Therefore, the InGaP with In composition of 0.5 is used to be the energy barrier layer of self-assembled InP ring-shaped QDMs in this work.

4.2 Monitoring of the InP Ring-shaped Quantum Dot Molecule Formation by *In Situ* RHEED.

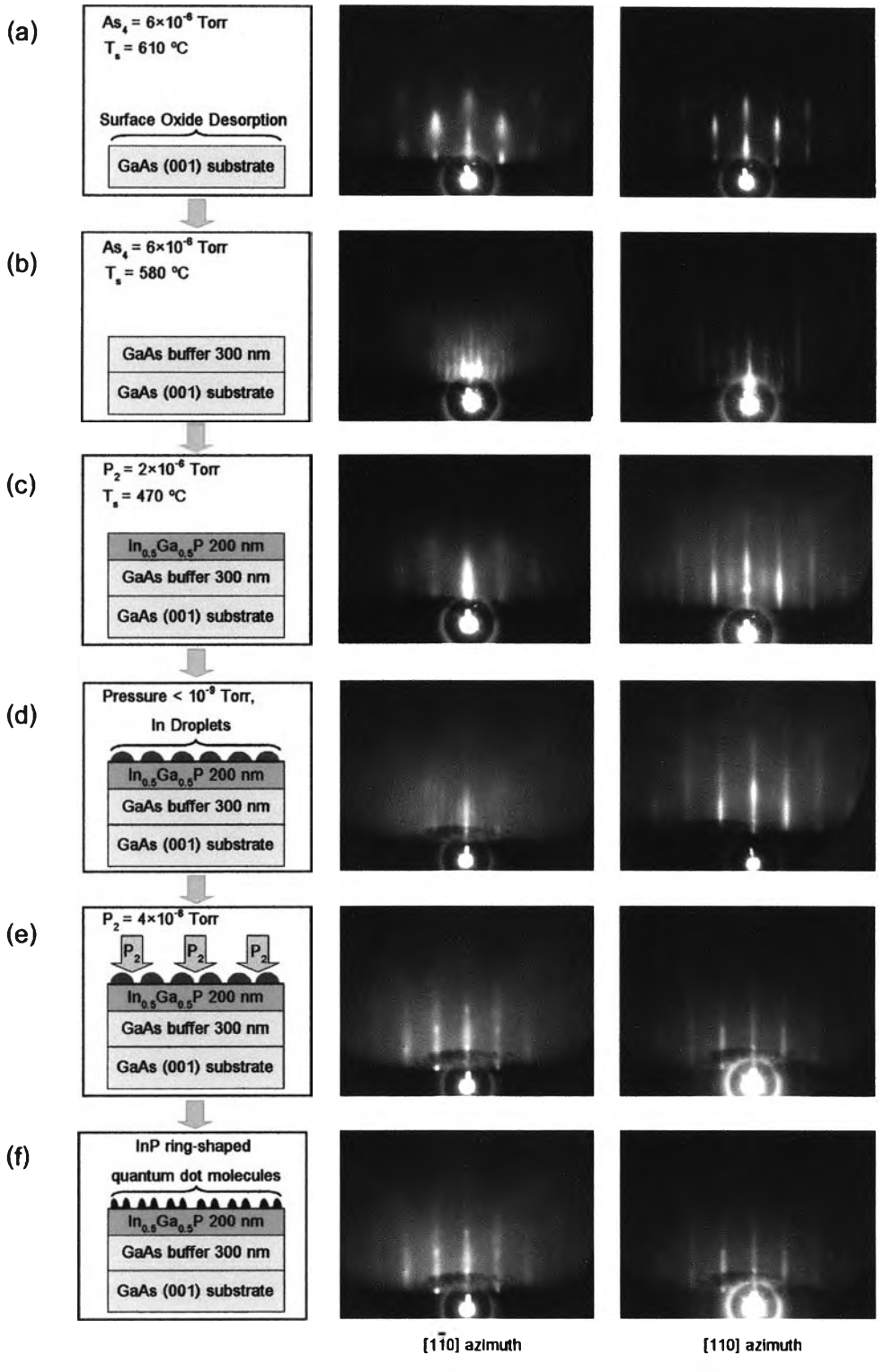

Figure 4.4 RHEED patterns of each experimental procedure in [1 $\bar{1}$0] azimuth and [110] azimuth.

The transition from a two-dimensional (2D) growth mode to a three-dimensional (3D) growth mode of ring-shaped QDM formation is illustrated by *in situ* recorded reflection high energy diffraction (RHEED) patterns in [$1\bar{1}0$] azimuth and [110] azimuth as shown in figure 4.4. During the surface oxide desorption, RHEED patterns indicate rough surface (figure 4.4 (a)). This reveals that the Ga_2O_3 escapes from the surface at substrate temperature higher than 580 °C under As flux supply. After GaAs buffer growth (figure 4.4 (b)), the sharp and clear 2×4 RHEED patterns or streaky patterns representing the smooth 2D surface, are observed. During the growth of $In_{0.5}Ga_{0.5}P$ layer (figure 4.4 (c)), RHEED patterns show 2×1 surface reconstructions. These elongated streaks demonstrated the 2D characteristic of the smooth surface. After In deposition (figure 4.4 (d)), streaky patterns still can be observed. These are resulted from the appearance of the extremely low density of the liquid phase (In droplets) on the surface. During crystallization (figure 4.4 (e)), more and more spotty RHEED patterns developed. This observation implies that the 3D islands (QDs) start to nucleate on the surface. As a result of RHEED pattern transition, we can summarize that the self-assembled InP ring-shaped QDMs are formed during crystallization process (figure 4.4 (f)).

4.3 Possible Formation Mechanism of InP Ring-shaped Quantum Dot Molecules

Figure 4.5 shows a schematic model of the self-organized InP ring-shaped QDMs formation during crystallization under P_2 beam equivalent pressure. In the display of figure 4.5(a) during deposition process, In is deposited onto $In_{0.5}Ga_{0.5}P$ layer and creates the initial In droplet as well as two-dimensional InP thin layer by cooperating with the exceed P atoms on the surface. During crystallization process, the surface is covered with P atoms as shown in figure 4.5(b). In atoms isotropically migrate away from center to periphery of the droplet and attach to the nearest P atoms while P atoms also diffuse into the In droplet. Consequently, the ring-shaped nanostructure has been formed. In the meanwhile, the lattice mismatch between the InP and $In_{0.5}Ga_{0.5}P$ underneath layer gives stain to form InP QDs along the circumference of ring-shaped nanostructure. Therefore, the formation of the ring-shaped QDMs occurs as shown in figure 4.5(c).

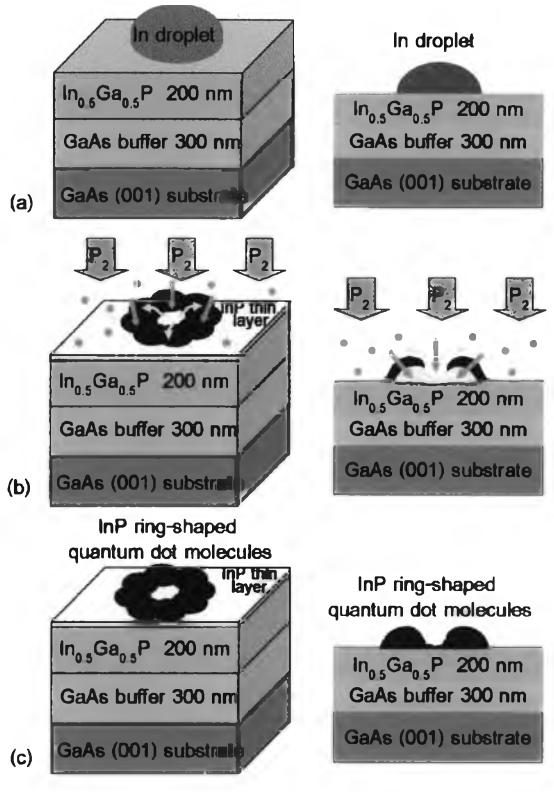

Figure 4.5 Schematic representations of the self-organized InP ring-shaped QDMs formation: (a) In droplet deposits on $In_{0.5}Ga_{0.5}P$ layer and creates the initial droplet with the InP thin layer. (b) during crystallization time, In migrates away from center to periphery of the droplet, P atoms diffuse into the droplet and the lattice mismatch between the InP and $In_{0.5}Ga_{0.5}P$ layer form the QDMs structure (c).

4.4 Effect of Deposition Temperature on the Properties of InP Ring-shaped Quantum Dot Molecules

In this work, the InP ring-shaped QDMs are realized by systematically tuning the growth conditions such as substrate temperature during deposition of In and crystallization, In deposition rate and amount of In deposition or In thickness. The first parameter studied for the formation and properties of InP ring-shaped QDMs is deposition temperature. Moritz et al. (1996), Kurtenbach et al. (1996), Zundel et al. (1998), Jin-phillipp and Phillipp (2000) proposed that formation of small InP islands and coherent dots initially occurs after InP deposition of approximately 1.5 monolayer (ML) and 3 ML, respectively Therefore, the initial controlled parameters in this experiment

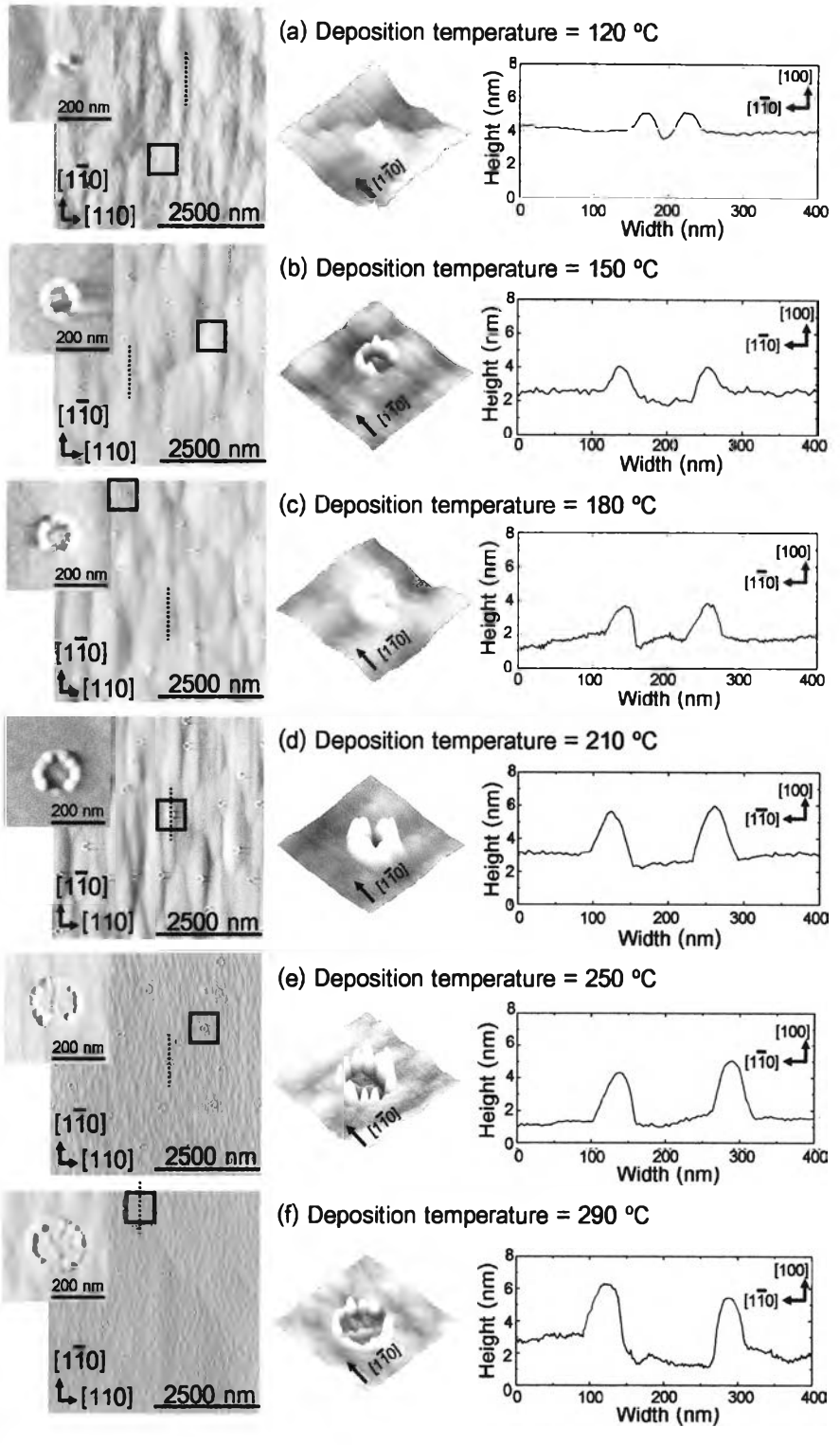

Figure 4.6 The 2D top-view and 3D tiled-view AFM images and cross-sectional line-profiles along [1 $\bar{1}$0] of InP ring-shaped QDMs formed at different deposition temperature of (a) 120°C (b) 150°C (c) 180°C (d) 210°C (e) 250°C and (f) 290°C and crystallization at 200°C. The 3.2-ML thick indium coverage was deposited at a rate of 0.8 ML/s.

were indium deposition rate of 0.8 ML/s, indium thickness of 3.2 ML, crystallization temperature at 200 °C under P_2 flux of 4×10^{-6} Torr for 5 minutes and the adjusting of deposition temperature from 120 °C-290 °C. Figure 4.6, observed by AFM, shows the dependence of surface morphology on the various substrate temperature of (a) 120 °C, (b) 150 °C, (c) 180 °C, (d) 210 °C, (e) 250 °C and (f) 290 °C during indium deposition. The 0.4×0.4 μm^2 and 5×5 μm^2 2D and 0.4×0.4 μm^2 3D AFM images and 400 nm cross-sectional line-profiles along $[1\bar{1}0]$ clearly display the ring-shaped QDM structures in all conditions.

The dependences of QD density, ring-shaped QDM density and outer/inner diameters of ring-shaped QDMs on the deposition temperature are shown in figure 4.7. The densities of QDs and ring-shape QDMs vary between 4.9×10^{8}-1.4×10^{9} cm^{-2} and 5.2×10^{7}-7.4×10^{8} cm^{-2}. The average outer and inner diameters of ring-shape QDMs vary between 84.1-228.9 nm and 23.5-126.3 nm. Increasing the deposition temperature reduces densities but enlarges average diameters.

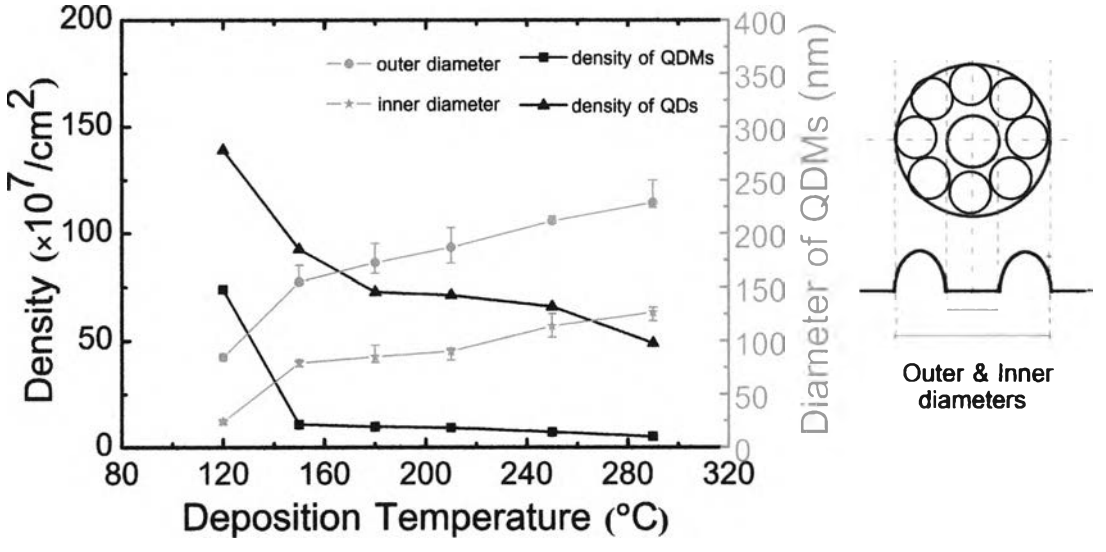

Figure 4.7 The dependence of InP QDs and ring-shaped QDMs densities and average outer and inner diameters of InP ring-shaped QDMs on the deposition temperature.

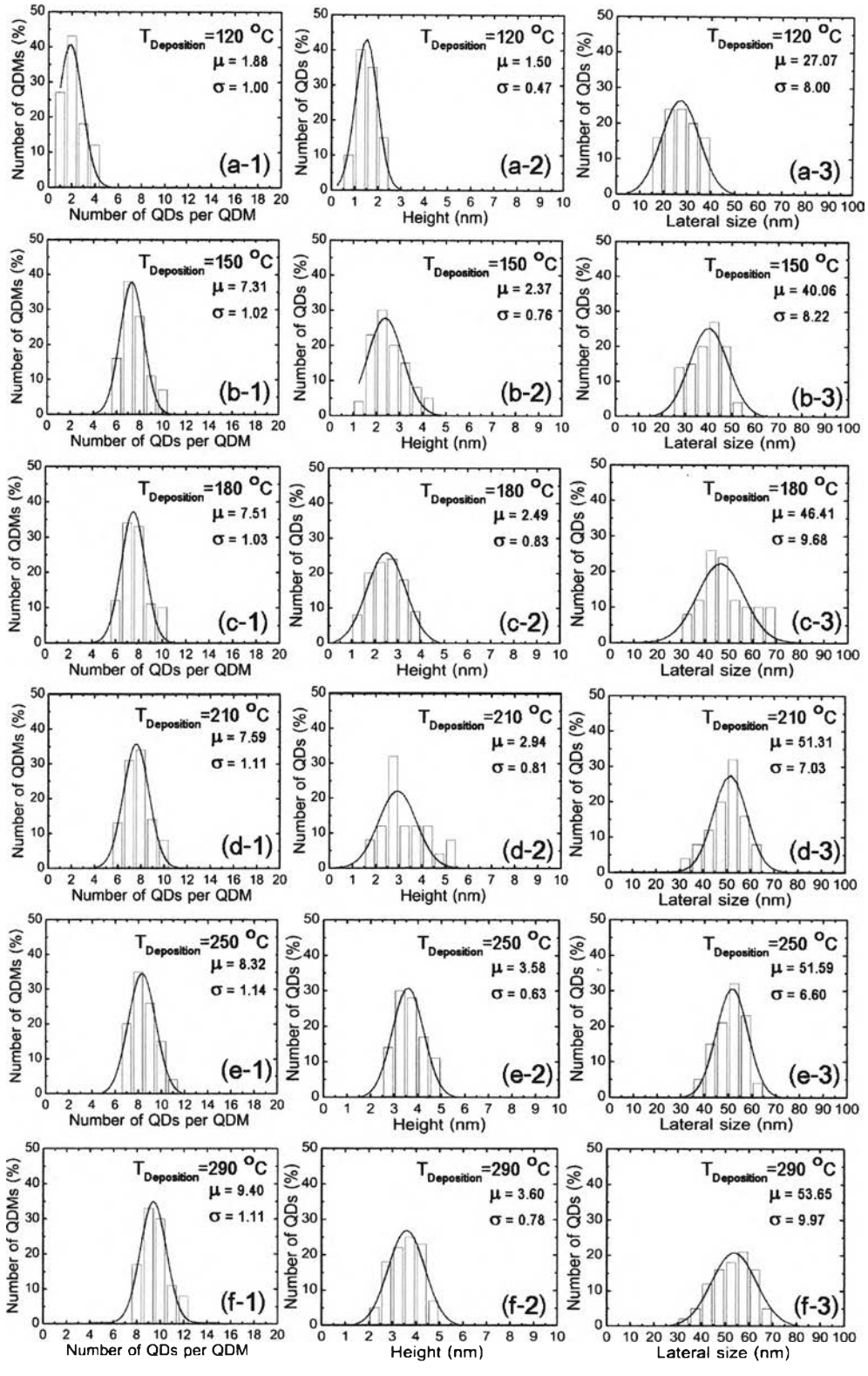

Figure 4.8 Distributions of the number of InP QDs per InP ring-shaped QDM ((a-f)-1), height ((a-f)-2) and lateral size of InP QDs ((a-f)-3) with various deposition temperatures.

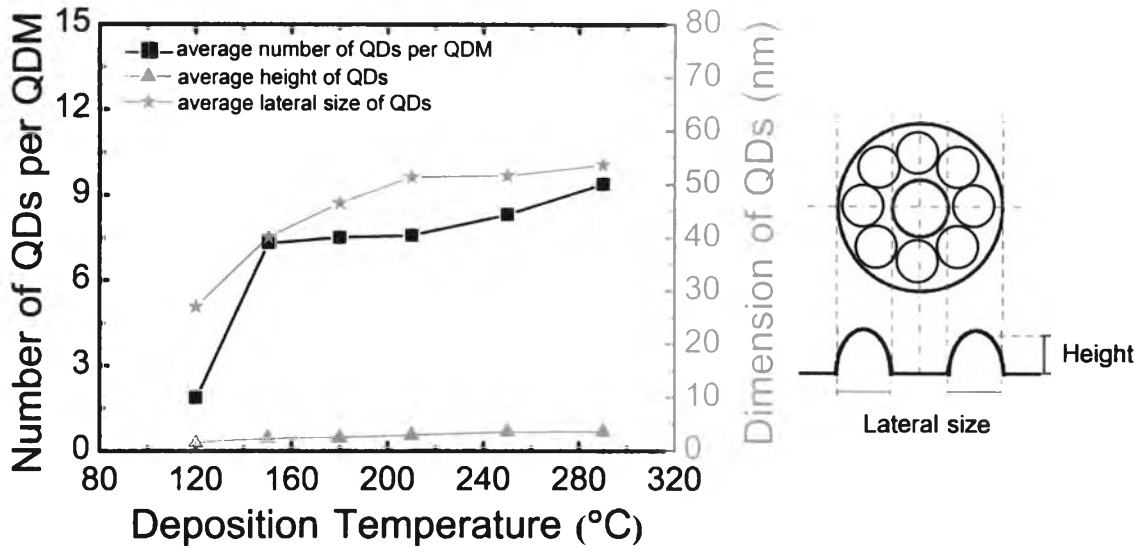

Figure 4.9 The dependence of the number of InP QDs per InP ring-shaped QDM, height and lateral size of InP QDs on the deposition temperature.

The distributions of number of QDs per QDM, height of QDs and lateral size of QDs which are fitted with the Gaussian distributions are shown in figure 4.8. All of average values of them are larger when the deposition temperature rises. The average number of QDs per QDM, average height of QDs and average lateral size of QD change between 1.9-9.4, 1.5-3.6 nm and 27.1-53.7 nm, respectively. The tendencies of ring-shaped QDMs properties are summarized in figure 4.9.

From these results, we can consider that only the densities of QDs and ring-shaped QDM are lower while the number of QDs per ring-shaped QDM and the dimensions of QD and ring-shaped QDM are larger at higher deposition temperature. These can be explained by the different energy consumption for initial In droplet formation. At higher deposition temperature, deposited In droplet acquires the higher thermal energy, resulting in more In displacement and consolidation. The cluster of small In droplets can more efficiently move, incorporate with each other to minimize the energy of system forming bigger initial In droplets and contribute to bigger QDs and ring-shaped QDMs. Hence, the deposition at high substrate temperature give larger sizes QDs and ring-shaped QDMs compared to the lower one. Corresponding to material conservation, the low density of QDs and ring-shaped QDMs are achieved from high deposition temperature.

As mentioned in chapter 3, the average size of QDs determines the peak energy level in the PL spectrum. Moreover, the PL linewidth or FWHM relates to the crystal quality and size distribution of QD array. In order to investigate the crystal quality and the homogeneity of QD, all ring-shaped QDM samples with different deposition temperature after crystallization were capped with 100-nm-thick $In_{0.5}Ga_{0.5}P$ layers using two-step growth. First, a 10-nm-thick $In_{0.5}Ga_{0.5}P$ was grown by migration enhanced epitaxy (MEE) technique at 300 °C with 0.5-ML/cycle growth rate. Then a 90-nm-thick $In_{0.5}Ga_{0.5}P$ was grown by conventional epitaxy growth at 470 °C with 0.5-ML/s growth rate. Before capping, temperature effect on the sample surface was observed by ramping the substrate temperature from 200 °C, crystallization process, to 250 °C, 300 °C and 350 °C as shown in figure 4.10. The higher temperature is mandatory to achieve high crystal quality layer, but increases small hillocks on the surface as a drawback after the temperature toward 350°C. Therefore, the first capping process by MEE technique is used and the temperature is chosen at 300 °C. After capping, all samples are measured by the macro-PL system at 20 K using a 478-nm line Ar^+ laser with 40 mW excitation power and the micro-PL system at room temperature using a 532-nm line diode-pumped solid state laser with 150 mW excitation power. The PL spectra of ring-shaped QDM samples are shown in figure 4.11 and 4.12. Although the PL spectra of both systems can not be directly compared due to the different of both excitation power and system setting, the tendencies of PL intensity and FWHM from both systems understandably reveal the effect of each growth parameter on InP ring-shaped QDM formation. The PL peaks which correspond to $In_{0.5}Ga_{0.5}P$, ground-state of InP ring-shaped QDMs and GaAs are resolved at 1.93 eV, 1.67-1.79 eV and 1.51 eV at 20 K and 1.85eV, 1.60-1.72 eV and 1.42 eV at room temperature, respectively. The FWHMs of InP ring-shaped QDMs vary between 50-60 meV at 20K and 65-82 meV at room temperature. The ground-state PL peaks show the good crystal quality of InP ring-shaped QDMs. The PL peaks, PL intensities and FWHMs which correspond to the QD sizes, QD densities and QD uniformities are gradually redshifted, lowered and narrowed, respectively by increasing the deposition temperature from 120 °C to 250 °C that agree with the extracted QD sizes, QD densities and size distributions from AFM measurements.

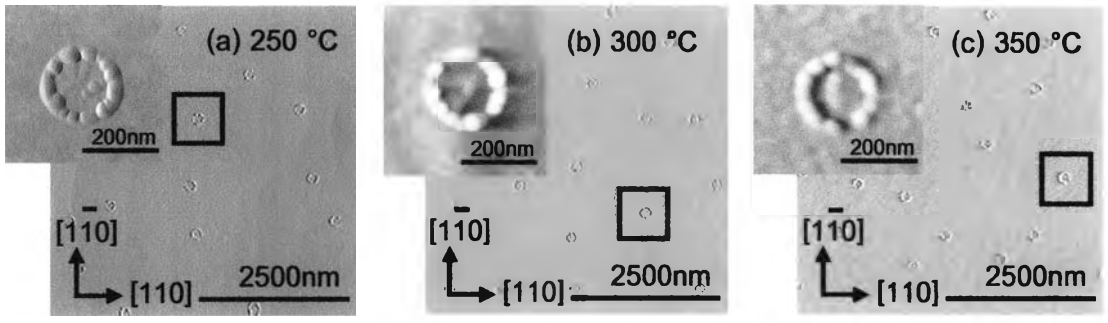

Figure 4.10 The 2D top-view AFM images of InP ring-shaped QDMs formed at deposition temperature of 250 °C, the crystallization temperature of 200 °C, the In deposition rate of 0.8 ML/s and the In deposition rate of 3.2 ML with different substrate temperature ramping of (a) 250°C (b) 300°C and (c) 350°C after crystallization.

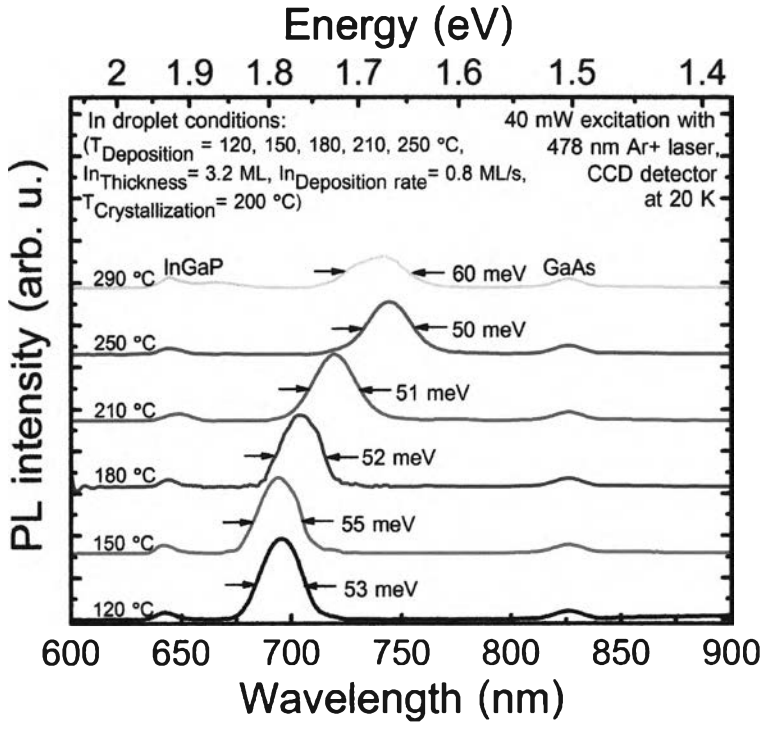

Figure 4.11 PL spectra of InP ring-shaped QDMs with various deposition temperatures measured by the macro-PL system at 20 K.

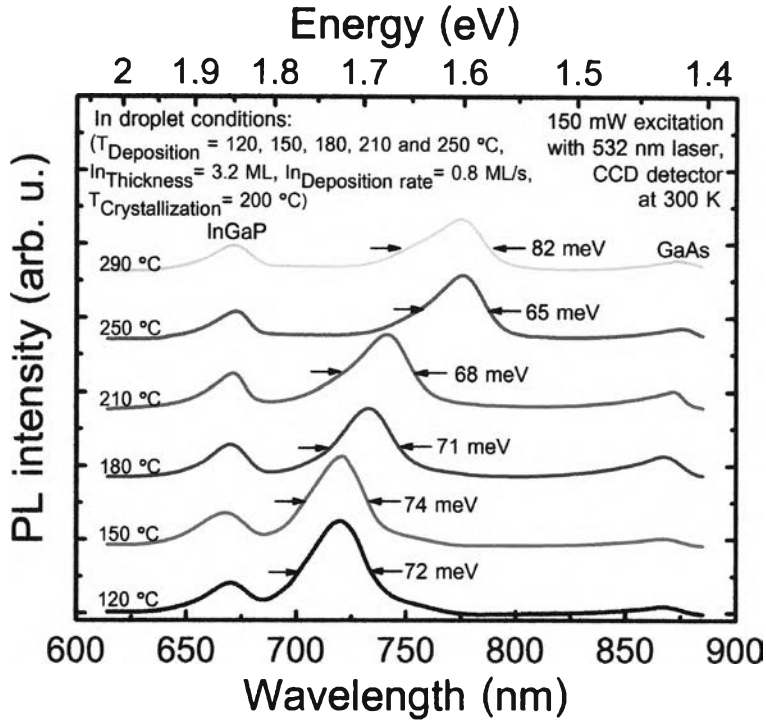

Figure 4.12 PL spectra of InP ring-shaped QDMs with various deposition temperatures measured by the micro-PL system at room temperature.

These FWHMs indicate that, from 120 °C to 250 °C, the uniformity of ring-shape QDMs becomes better at higher deposition temperature. However, at the highest deposition temperature in this experiment at 290 °C, the FWHM is broadened due to the worse QD homogeneity. Therefore, in order to investigate other parameters, deposition temperature will be fixed at 250 °C because the best QD size uniformity and the highest number of QDMs (35%) which consist of eight QDs per QDM could be achieved at this deposition temperature.

4.5 Effect of Crystallization Temperature on the Properties of InP Ring-shaped Quantum Dot Molecules

The second parameter studied for the formation and properties of InP ring-shaped QDMs is crystallization temperature. The other controlled parameters are deposition temperature at 250 °C, indium deposition rate of 0.8 ML/s, indium thickness of 3.2 ML and crystallization under P_2 flux of 4×10^{-6} Torr for 5 minutes. Figure 4.13, observed by

AFM, shows the dependence of surface morphology on the various crystallization temperature of (a) 150 °C, (b) 200 °C, (c) 250 °C and (d) 300 °C. The 0.4×0.4 μm^2 and 5×5 μm^2 2D and 0.4×0.4 μm^2 3D AFM images and 400 nm cross-sectional line-profiles along [1 $\bar{1}$0] display the ring-shaped QDM structures in all conditions.

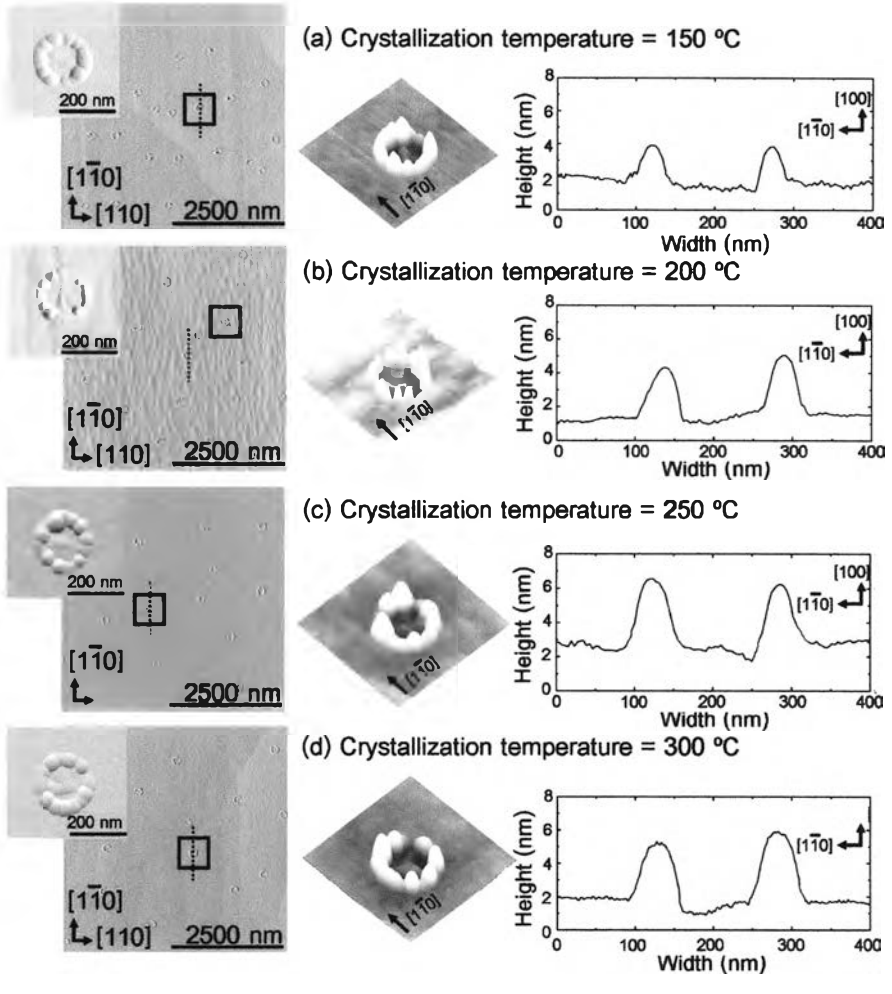

Figure 4.13 The 2D top-view and 3D tiled-view AFM images and cross-sectional line-profiles along [1 $\bar{1}$0] of InP ring-shaped QDMs formed at different crystallization temperature of (a) 150°C (b) 200°C (c) 250°C and (d) 300°C. The deposition temperature was 200°C with coverage of 3.2 ML indium droplet and indium deposition rate of 0.8 ML/s.

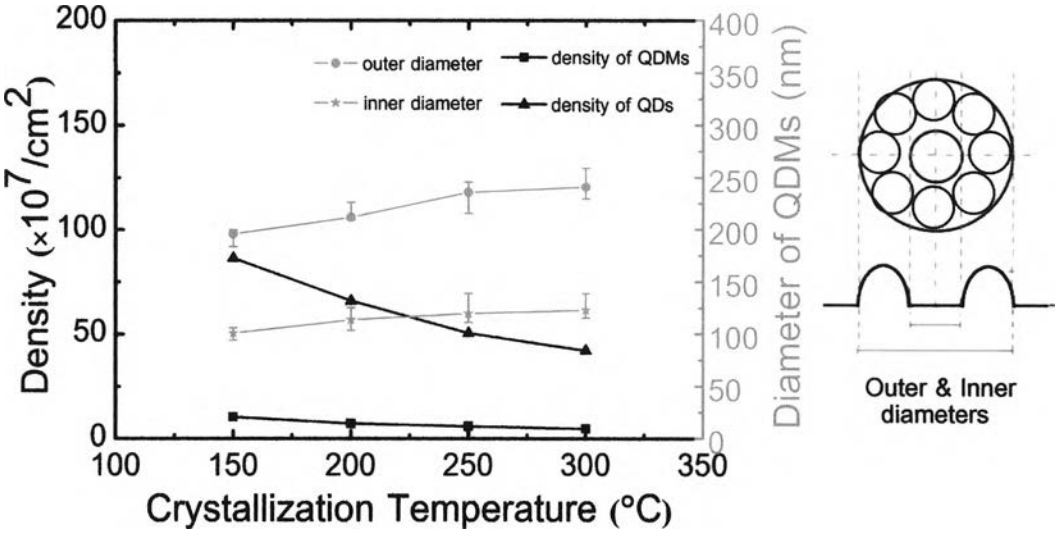

Figure 4.14 The dependence of InP QDs and ring-shaped QDMs densities and average outer and inner diameters of InP ring-shaped QDMs on the crystallization temperature.

The summaries of QD densities, ring-shaped QDM densities and outer/inner diameters of ring-shaped QDMs as functions of the crystallization temperature are shown in figure 4.14. The densities of QDs and ring-shape QDMs vary between 4.2×10^{8}-8.6×10^{8} cm^{-2} and 4.8×10^{7}-1.1×10^{8} cm^{-2}. The average outer and inner diameters of ring-shape QDMs vary between 195.5-240.8 nm and 100.4-122.9 nm. Increasing the crystallization temperature reduces densities but enlarges average diameters.

The distributions of number of QDs per QDM, height of QDs and lateral size of QDs which are fitted with the Gaussian distributions are shown in figure 4.15. All of average values are larger when the crystallization temperature rises. The average number of QDs per QDM, average height of QDs and average lateral size of QD change between 8.3-8.8 nm, 2.3-4.0 nm and 42.4-53.4 nm, respectively. The tendencies of these parameters are summarized in figure 4.16.

According to these results, it is considerable that only the densities of QDs and ring-shaped QDMs are lessened while the number of QDs per ring-shaped QDM and the dimensions of QD and ring-shaped QDM are added at higher crystallization temperature. The tendencies of these resultants are as similar as the experiment of deposition temperature in which the sizes of QDs become larger corresponding to the lowering of ring-shaped QDMs density at higher substrate temperature. These can be specifically

explained that, in the case of the crystallization temperature is lower than deposition temperature; the lower crystallization temperature can more restrain the displacement and incorporation of In droplet, contributing the smaller QDs and ring-shaped QDMs. In the case of the crystallization temperature is equal or higher than deposition temperature; the higher crystallization temperature can more efficiently activate the deposited In droplet to farther movement and incorporating with each other to minimize the energy of system and contributing to bigger QDs and ring-shaped QDMs. Corresponding to material conservation, the low density of QDs and ring-shaped QDMs are achieved from high crystallization temperature.

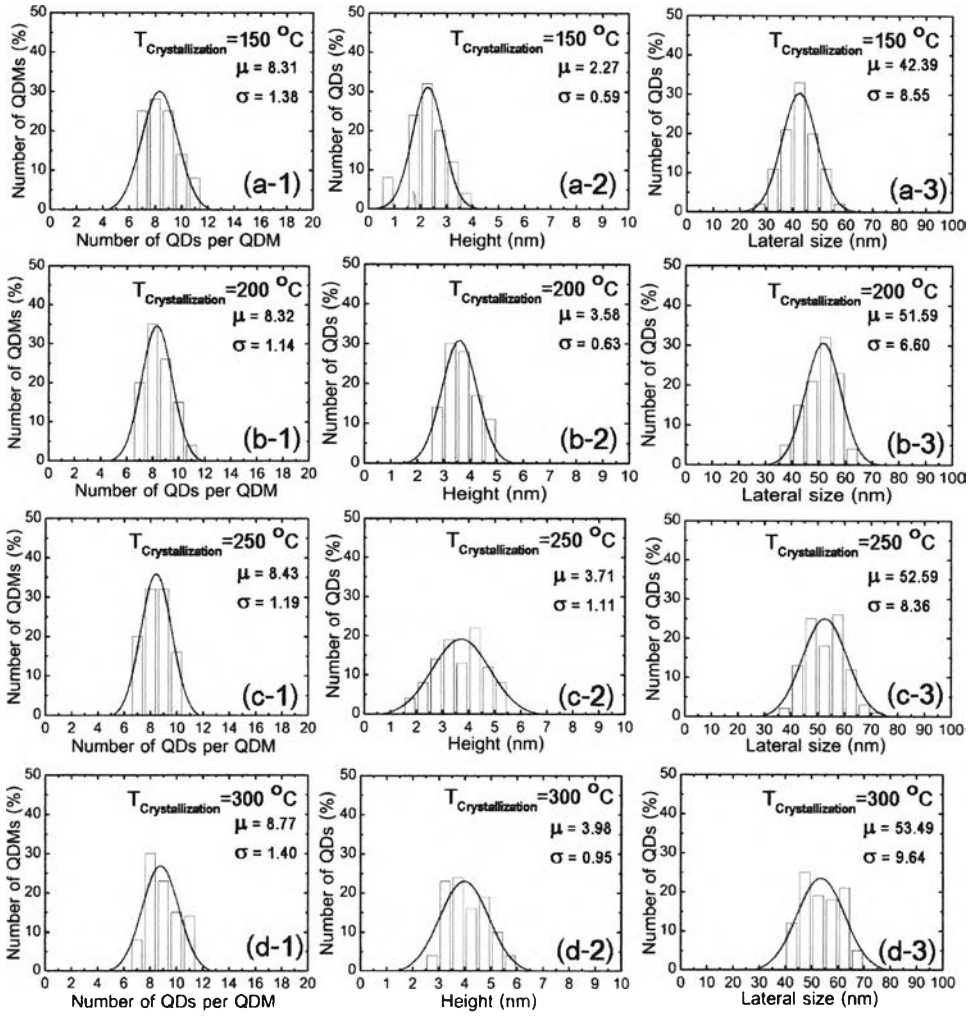

Figure 4.15 Distributions of the number of InP QDs per InP ring-shaped QDM ((a-d)-1), height ((a-d)-2) and lateral size of InP QDs ((a-d)-3) with various crystallization temperatures.

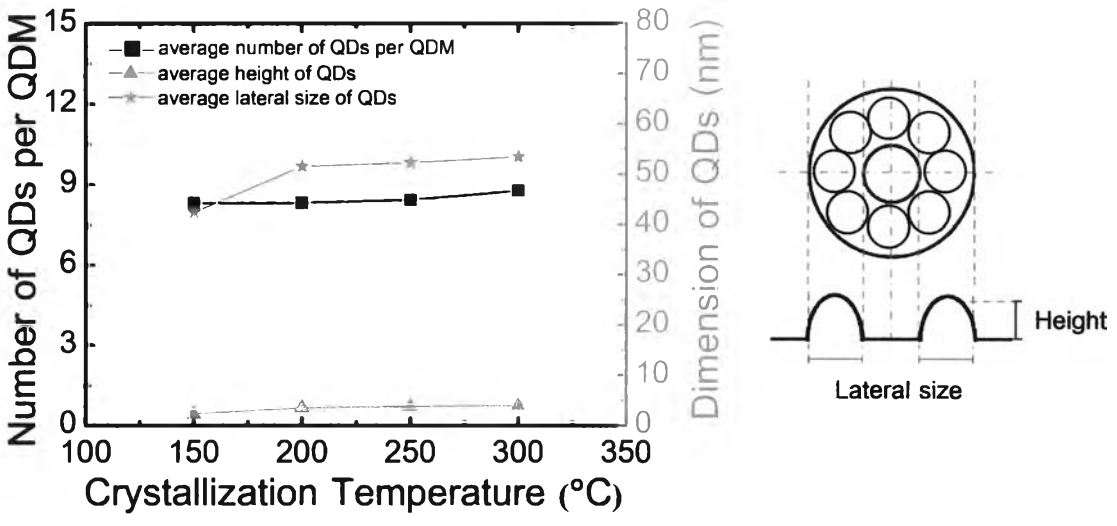

Figure 4.16 The dependence of the number of InP QDs per InP ring-shaped QDM, height and lateral size of InP QDs on the crystallization temperature.

In order to investigate the crystal quality and the uniformity of QD, all ring-shaped QDM samples with different crystallization temperature are measured by the macro-PL system at 20 K and the micro-PL system at room temperature. The PL spectra of ring-shaped QDM samples are shown in figure 4.17 and 4.18. The PL peaks of $In_{0.5}Ga_{0.5}P$, ground-state of InP ring-shaped QDMs and GaAs are resolved at 1.93 eV, 1.64-1.78 eV and 1.51 eV at 20 K and 1.85 eV, 1.57-1.71 eV and 1.42 eV at room temperature, respectively. The FWHMs of InP ring-shaped QDMs vary between 50-55 meV at 20 K and 65-71 meV at room temperature. The ground-state PL peaks show the good crystal quality of InP ring-shaped QDMs. The PL peaks, PL intensities and FWHMs which correspond to the QD sizes, QD densities and QD homogeneities are gradually redshifted, lowered and narrowed, respectively by increasing the crystallization temperature from 150 °C to 200 °C that agree with the extracted QD sizes, QD densities and size distributions from AFM measurements. These FWHMs reveal that the uniformity of ring-shape QDMs becomes better at higher crystallization temperature from 150 °C to 200 °C. However, for higher crystallization temperature at 250 °C and 300 °C, the FWHMs are broadened due to the worse QD homogeneity. Therefore, in order to investigate next parameters, deposition temperature and crystallization temperature will be fixed at 250 °C and 200 °C because the best QD size and uniformity and the highest number of QDMs (35%) which consist of eight QDs per QDM could be achieved at these deposition and crystallization temperatures.

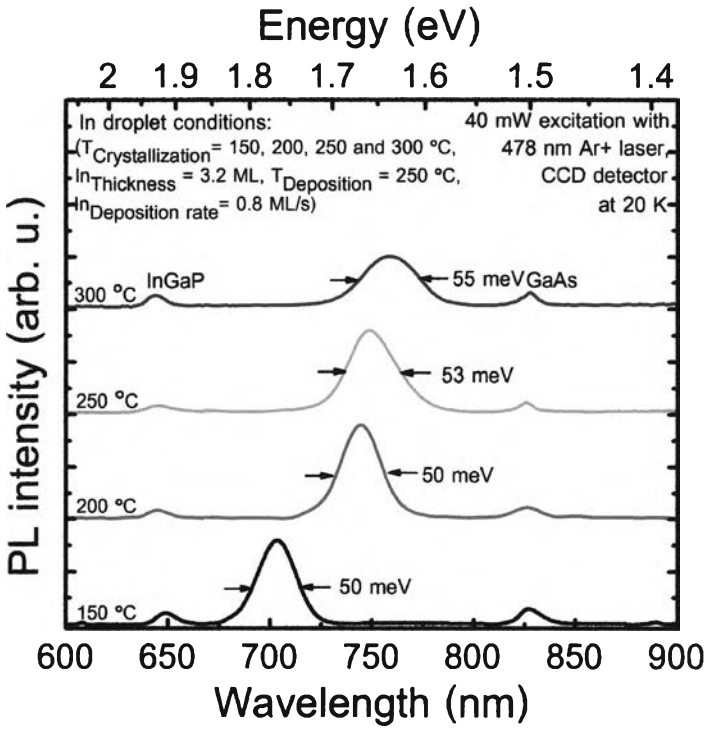

Figure 4.17 PL spectra of InP ring-shaped QDMs with various crystallization temperatures measured by the macro-PL system at 20 K.

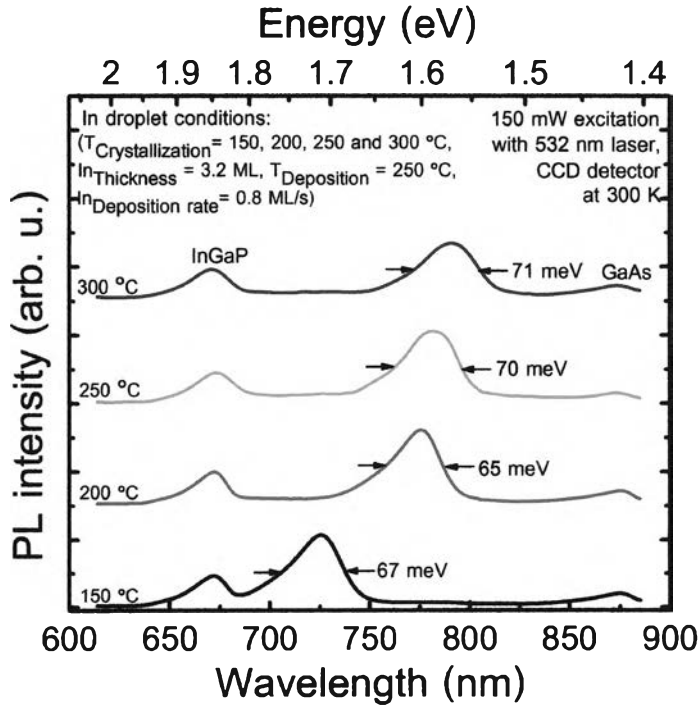

Figure 4.18 PL spectra of InP ring-shaped QDMs with various crystallization temperatures measured by the micro-PL system at room temperature.

As the results of these experiments, we can summarize that the deposition temperature and crystallization temperature have similar effects on the physical and optical properties of InP ring-shaped QDMs. However, the effect of deposition temperature is remarkably stronger than the other because the QD and ring-shaped QDM sizes are mainly determined during the deposition and slightly transform by the crystallization process. The crystallization temperature which is a little bit lower than deposition temperature gives the good QD quality.

4.6 Effect of Indium Deposition Rate on the Properties of InP Ring-shaped Quantum Dot Molecules

The third parameter studied for the formation and properties of InP ring-shaped QDMs is In deposition rate. The other controlled parameters are deposition temperature at 250 °C, indium thickness of 3.2 ML and crystallization temperature at 200 °C under P_2 flux of 4×10^{-6} Torr for 5 minutes. The samples were evaluated in the same manner with the previous experiments. AFM images in figure 4.19 display the dependence of surface morphology on the various indium deposition rate of (a) 0.2 ML/s (b) 0.4 ML/s, (c) 0.8 ML/s and (d) 1.6 ML/s. The 0.4×0.4 μm^2 and 5×5 μm^2 2D and 0.4×0.4 μm^2 3D AFM images and 400 nm cross-sectional line-profiles along $[1\bar{1}0]$ show the ring-shaped QDM structures in all conditions.

The dependences of QD density, ring-shaped QDM density and outer/inner diameters of ring-shaped QDMs on the indium deposition rate are shown in figure 4.20. The densities of QDs and ring-shape QDMs vary between 4.1×10^{8}-8.3×10^{8} cm^{-2} and 3.6×10^{7}-1.0×10^{8} cm^{-2}. The average outer diameter and average inner diameter of ring-shape QDMs varies between 186.1-273.3 nm and 106.9-143.6 nm. Increasing the indium deposition rate enlarges densities but reduces average diameters.

The distributions of number of QDs per QDM, height of QDs and lateral size of QDs which are fitted with the Gaussian distributions are shown in figure 4.21. All average values of them are smaller when the indium deposition rate rises. The average number of QDs per QDM, average height of QDs and average lateral size of QD change between 8.3-11.5 nm, 3.5-3.7 nm and 44.0-55.0 nm, respectively. The tendencies of each parameter are summarized in figure 4.22.

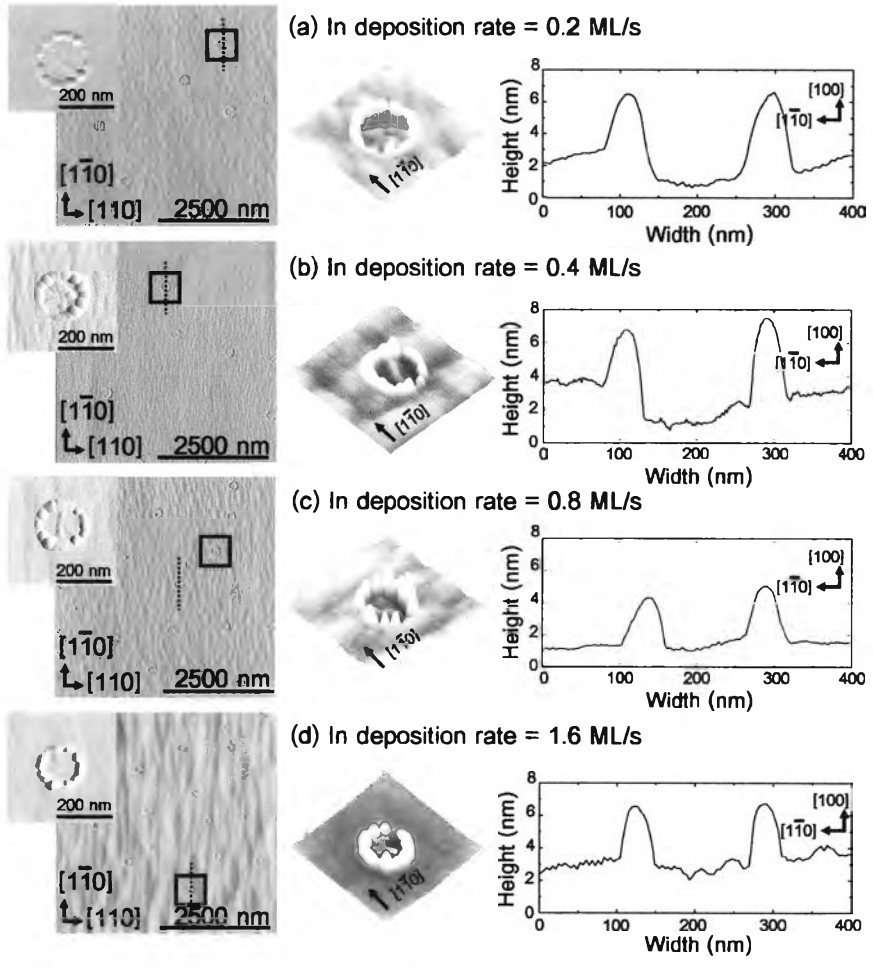

Figure 4.19 The 2D top-view and 3D tiled-view AFM images and cross-sectional line-profiles along [1$\bar{1}$0] of InP ring-shaped QDMs formed at different indium deposition rate of (a) 0.2 ML/s (b) 0.4 ML/s, (c) 0.8 ML/s and (d) 1.6 ML/s. The deposition and crystallization temperature were 250°C and 200°C with coverage of 3.2 ML indium droplet and indium deposition rate of 0.8 ML/s.

From these results, it is obvious that only the QDs and ring-shaped QDM are denser while the number of QDs per ring-shaped QDM and the dimensions of QD and ring-shaped QDM are lower at higher indium deposition rate. These can be explained by the different time scale for initial In droplet formation. For a lower deposition rate, initial In droplet formation is put into a extended time interval, resulting in more In displacement and consolidation. The cluster of small In droplets can more efficiently move, incorporate with each other to minimize the energy of system forming bigger initial

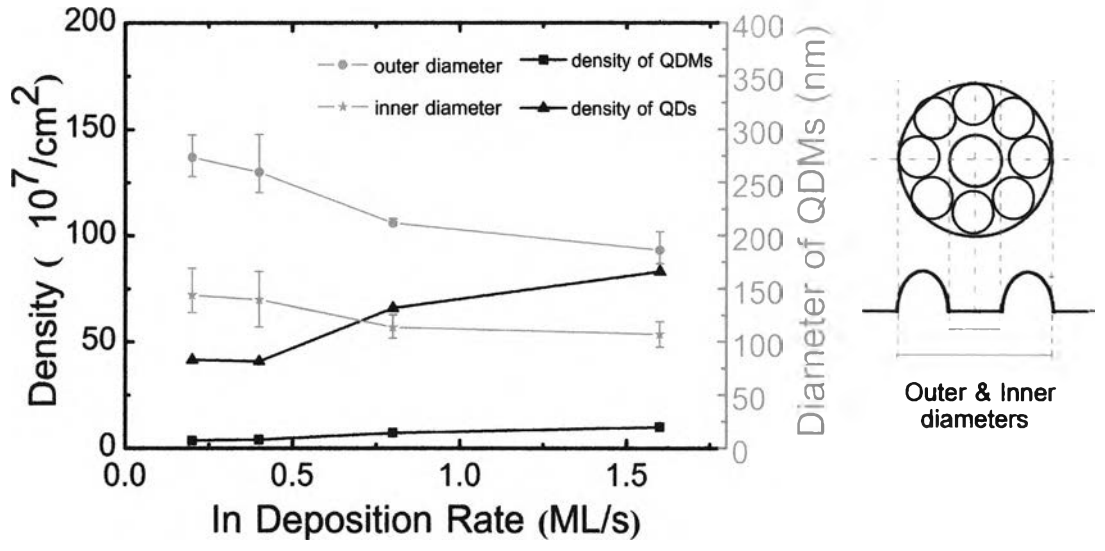

Figure 4.20 The dependence of InP QDs and ring-shaped QDMs densities and average outer and inner diameters of InP ring-shaped QDMs on the indium deposition rate.

In droplets and contribute to bigger QDs and ring-shaped QDMs. Corresponding to material conservation, the low density of QDs and ring-shaped QDMs from deposition at low growth rate must have larger sizes compared with deposition at higher growth rate.

All ring-shaped QDMs samples fabricated with different In deposition rate are examined by the macro-PL system at 20 K and the micro-PL system at room temperature in order to investigate the crystal quality and the uniformity of QD. The PL spectra of ring-shaped QDM samples are shown in figure 4.23 and 4.24. The PL peaks of $In_{0.5}Ga_{0.5}P$, ground-state of InP ring-shaped QDMs and GaAs are resolved at 1.93 eV, 1.64-1.68 eV and 1.51 eV at 20 K and 1.85 eV, 1.58-1.61 eV and 1.42 eV at room temperature, respectively. The ground-state PL peaks show the good crystal quality of InP ring-shaped QDMs. The PL peaks, PL intensities and FWHMs which correspond to the QD sizes, QD densities and QD homogeneities are gradually blueshifted, increased and narrowed, respectively by increasing the In deposition rate from 0.2 ML/s to 1.6 ML/s that agree with the extracted QD sizes, QD densities and size distributions from AFM measurements. These FWHMs values reveal that the uniformity of QDs and ring-shape QDMs becomes better at higher indium deposition rate. Although a high In deposition rate is preferred to achieve a better result, the indium deposition rate higher than 1.6 ML/s cannot be done in this work due to the limitation of beam equivalent

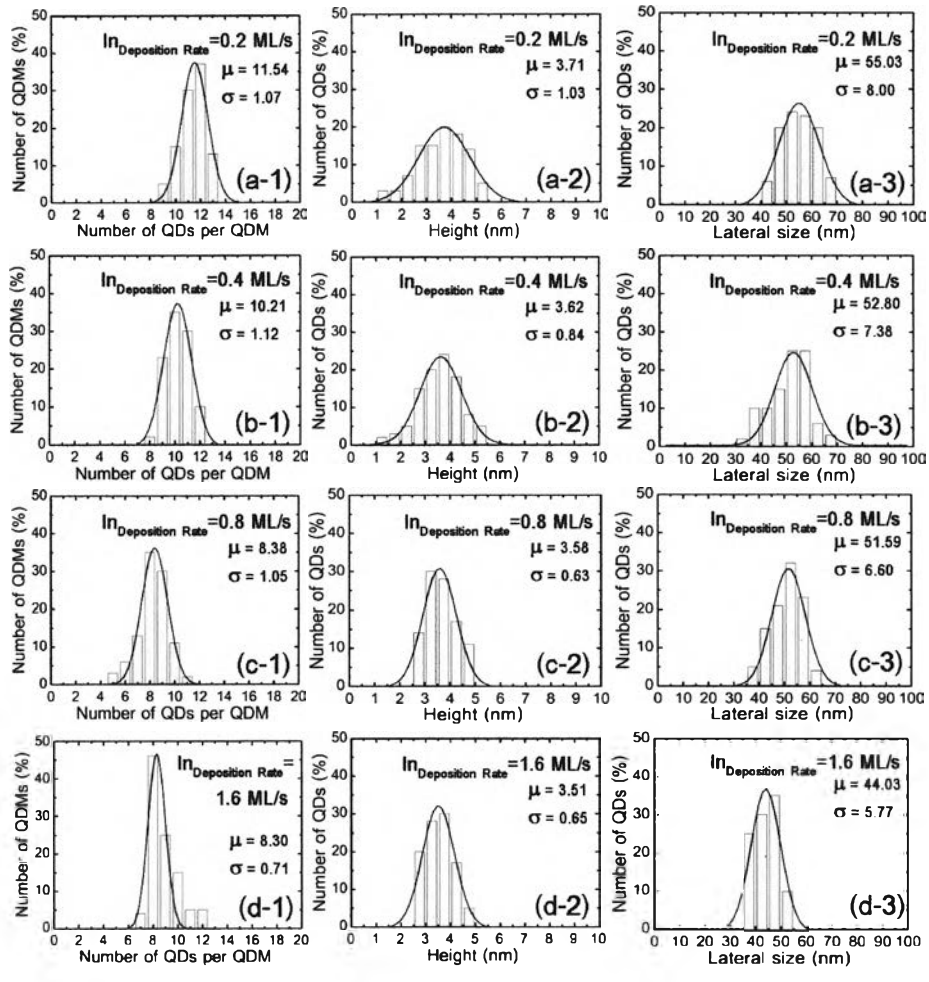

Figure 4.21 Distributions of the number of InP QDs per InP ring-shaped QDM ((a-d)-1), height ((a-d)-2) and lateral size of InP QDs ((a-d)-3) with various indium deposition rate.

pressure (BEP) or cell temperature (900 °C) of In source. Therefore, in order to investigate next parameters, deposition and crystallization temperature and In deposition rate will be fixed at 250 °C, 200 °C and 1.6 ML/s respectively because the best QD size and uniformity and the highest number of QDMs (46%) which consist of eight QDs per QDM could be achieved at these deposition temperature, crystallization temperature and In deposition rate.

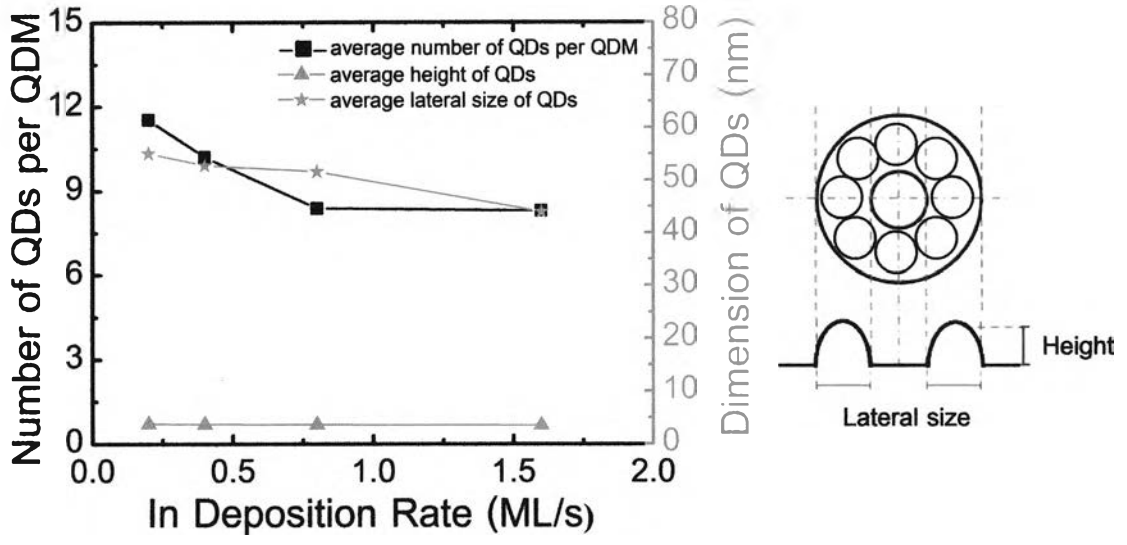

Figure 4.22 The dependence of the number of InP QDs per InP ring-shaped QDM, height and lateral size of InP QDs on the indium deposition rate.

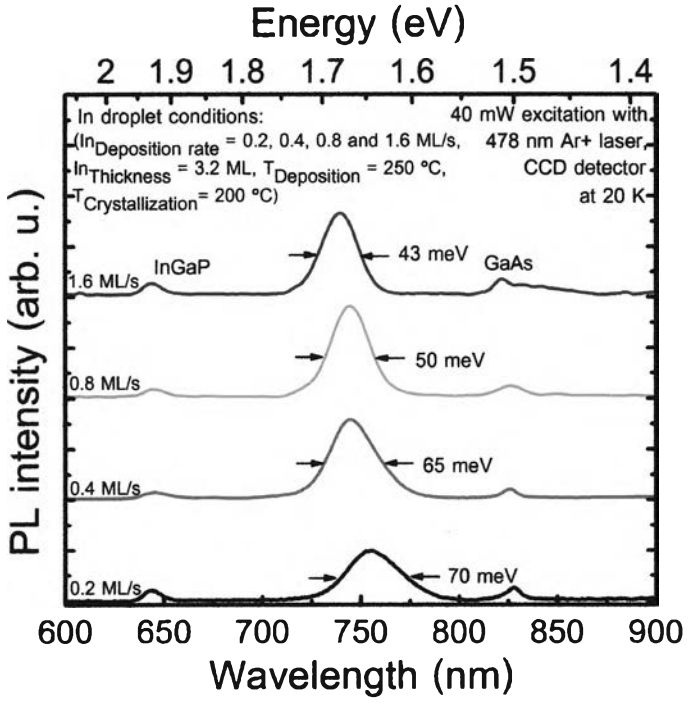

Figure 4.23 PL spectra of InP ring-shaped QDMs with various indium deposition rate measured by the macro-PL system at 20 K.

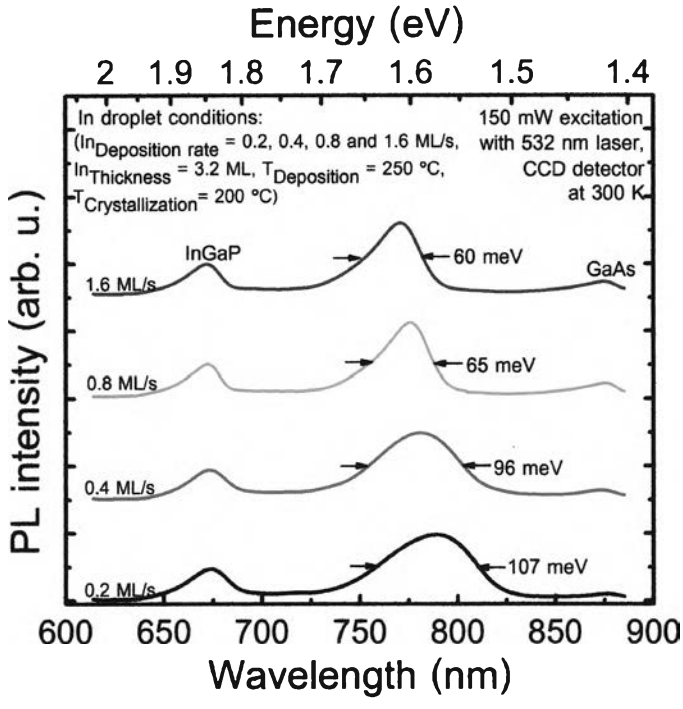

Figure 4.24 PL spectra of InP ring-shaped QDMs with various indium deposition rate measured by the micro-PL system at room temperature.

4.7 Effect of Indium Thickness on the Properties of InP Ring-shaped Quantum Dot Molecules

The last parameter studied for the formation and properties of InP ring-shaped QDMs in this work is In thickness using the optimized parameters from the previous experiments. Figure 4.25, observed by AFM, shows the dependence of surface morphology on the various In thickness of (a) 1.6 ML (b) 3.2 ML, (c) 4.8 ML and (d) 6.4 ML. The 0.4×0.4 μm^2 and 5×5 μm^2 2D and 0.4×0.4 μm^2 3D AFM images and 400 nm cross-sectional line-profiles along [1 $\bar{1}$0] clearly display the QR structure at In thickness of 1.6 ML and the ring-shaped QDM structures in other conditions.

The dependences of QR, QD, ring-shaped QDM densities and outer/inner diameters of QR and ring-shaped QDMs on the In thickness are shown in figure 4.26. The density of QRs is 1.0×10^8 cm^{-2} and the densities of QDs and ring-shaped QDMs vary between 8.3×10^8-1.1×10^9 cm^{-2} and 8.4×10^7-1.0×10^8 cm^{-2}. The average outer diameter and average inner diameter of QRs and ring-shape QDMs vary between 124.4-251.5 nm and

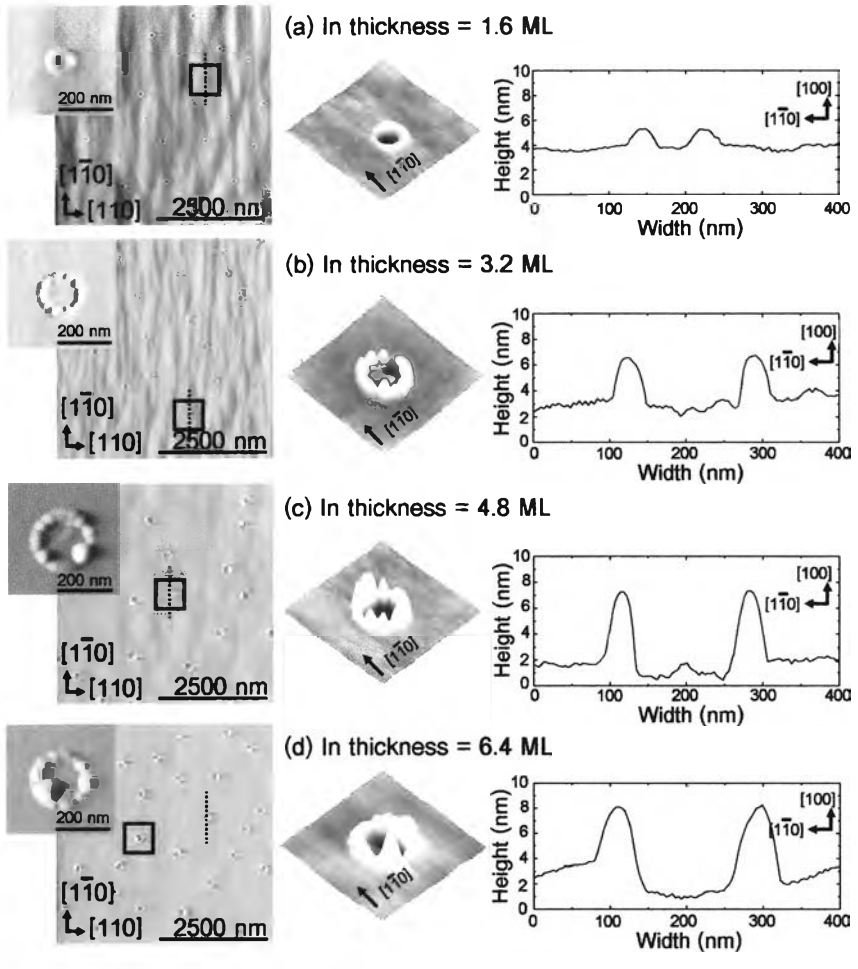

Figure 4.25 The 2D top-view and 3D tiled-view AFM images and cross-sectional line-profiles along [1 $\bar{1}$0] of InP ring-shaped QDMs formed at different indium thickness of (a) 1.6 ML (b) 3.2 ML, (c) 4.8 ML and (d) 6.4 ML. The deposition and crystallization temperature were 250°C and 200°C, respectively with indium deposition rate of 0.8 ML/s.

51.9-117.8 nm. Increasing the In thickness raises densities and enlarges average diameters.

The distributions of number of QDs per QDM, height and lateral size of QRs and QDs with the Gaussian fittings are shown in figure 4.27. All average values are larger when the In thickness rises. The average number of QDs per QDM, average height of and average lateral size of QRs and QDs change between 3.5-11.6 nm, 1.5-4.9 nm and 34.2-63.3 nm, respectively. The tendencies of them are summarized in figure 4.28.

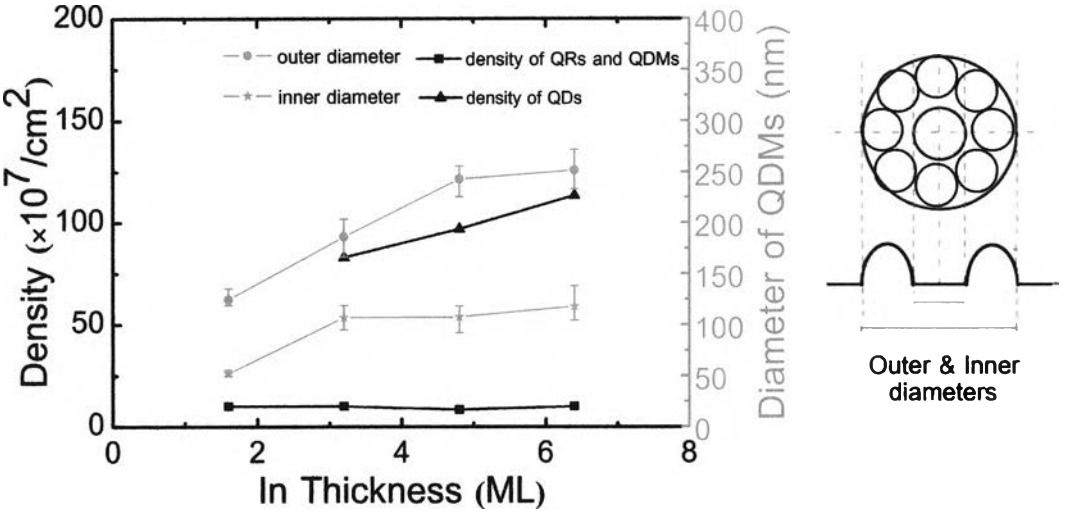

Figure 4.26 The dependence of InP QRs, QDs and ring-shaped QDMs densities and average outer and inner diameters of InP QRs and ring-shaped QDMs on the indium thickness.

According to the results, the densities of QDs and ring-shaped QDM, the number of QDs per ring-shaped QDM, the dimensions of QD and ring-shaped QDM at In thickness from 3.2 ML to 6.4 ML are increased with In thickness.

As similar with the other experiments, the samples grown with different In thickness were evaluated the crystal quality and the homogeneity via the PL measurements. The macro-PL and micro-PL spectra of QRs and ring-shaped QDM samples are shown in figure 4.29 and 4.30, respectively. The PL peaks which correspond to $In_{0.5}Ga_{0.5}P$, ground-state of InP ring-shaped QDMs and GaAs are resolved at 1.93 eV, 1.68-1.69 eV and 1.51 eV at 20 K and 1.85 eV, 1.60-1.62 eV and 1.42 eV at room temperature, respectively. The PL peaks which correspond to ground-state of InP QRs are resolved at 1.79 eV at 20 K and 1.72 eV at room temperature. The ground-state PL peaks show the good crystal quality of InP QRs and ring-shaped QDMs. The PL peaks, PL intensities and FWHMs of In thickness from 3.2 ML to 6.4 ML which correspond to the QD sizes, QD densities and QD homogeneities are gradually redshifted, increased and widened, respectively by increasing the In thickness that agree with the extracted QD sizes, QD densities and size distributions from AFM measurements. However, with In thickness of 4.8 ML and 6.4 ML, the FWHM is broadened and PL peak consist of two peaks because of the QD inhomogeneity attributing to two variations of QD height as

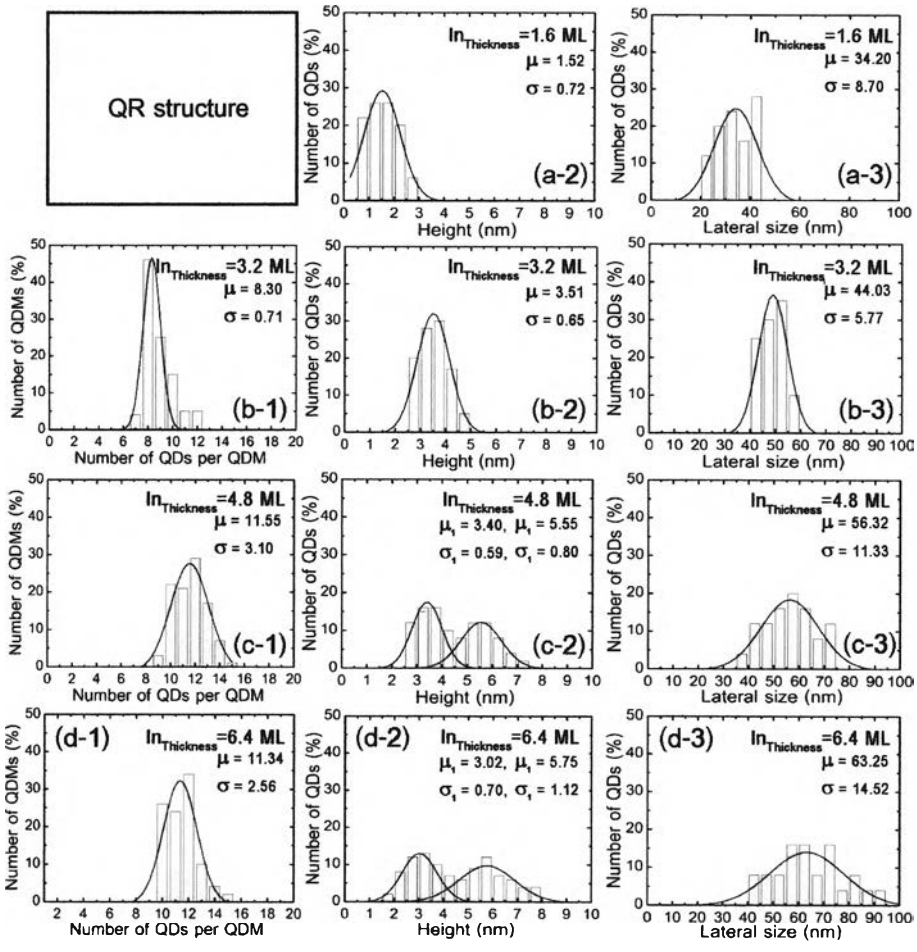

Figure 4.27 Distributions of the number of InP QDs per InP ring-shaped QDM ((b-d)-1), height ((a-d)-2) and lateral size of InP QRs and QDs ((a-d)-3) with various indium thickness.

shown in figure 4.27. Although the high In thickness is preferred for a high density and clear QDM structure, the QD homogeneities are worse when In thickness are 4.8 ML and higher than that giving the appropriate In thickness of around 3.2 ML. Therefore, the investigation of growth parameters in this work for InP ring-shaped QDMs formation can be concluded that the appropriate deposition temperature, crystallization temperature, In deposition rate and In thickness are 250 °C, 200 °C, 1.6 ML/s and 3.2 ML, respectively. The best QD size uniformity and the number of QDMs which consist of eight QDs per QDM as high as 46% could be achieved at this condition. The critical In thickness and In amount of coherent QD formation of this growth condition by droplet epitaxy technique in this work is between 1.6 ML-3.2 ML and 3.2 ML, respectively.

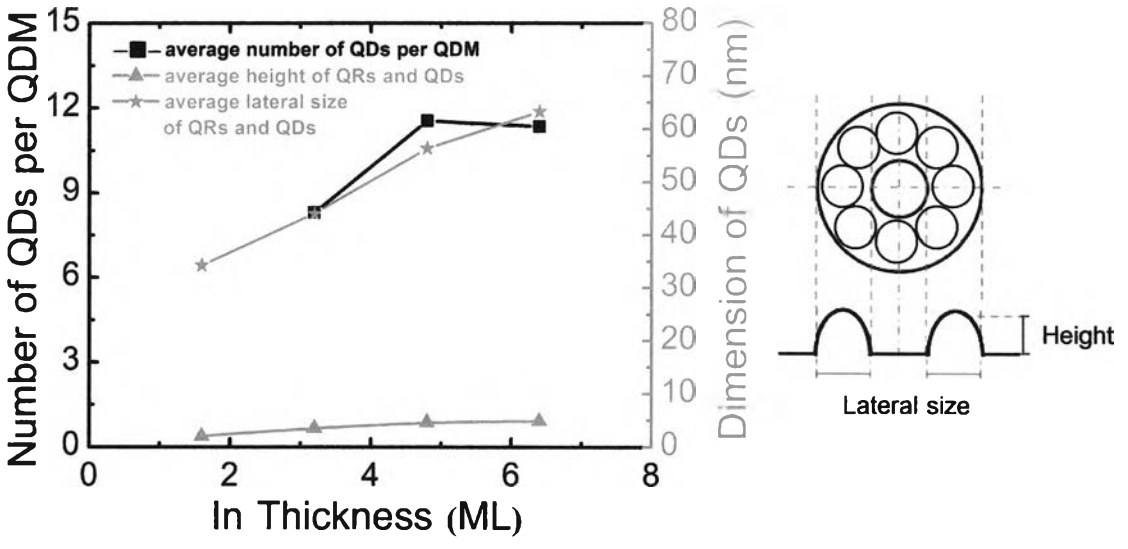

Figure 4.28 The dependence of the number of InP QDs per InP ring-shaped QDM, height and lateral size of InP QRs and QDs on the indium thickness

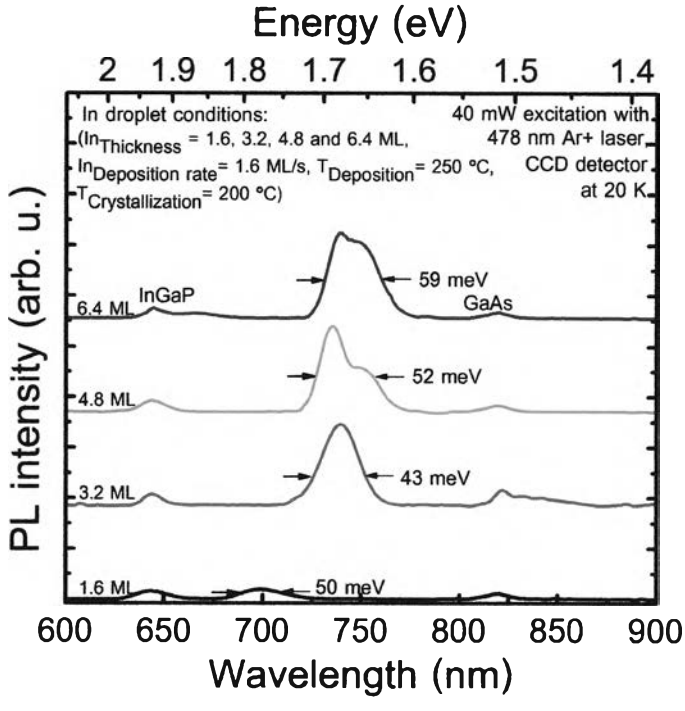

Figure 4.29 PL spectra of InP QRs and ring-shaped QDMs with various indium thickness measured by the macro-PL system at 20 K.

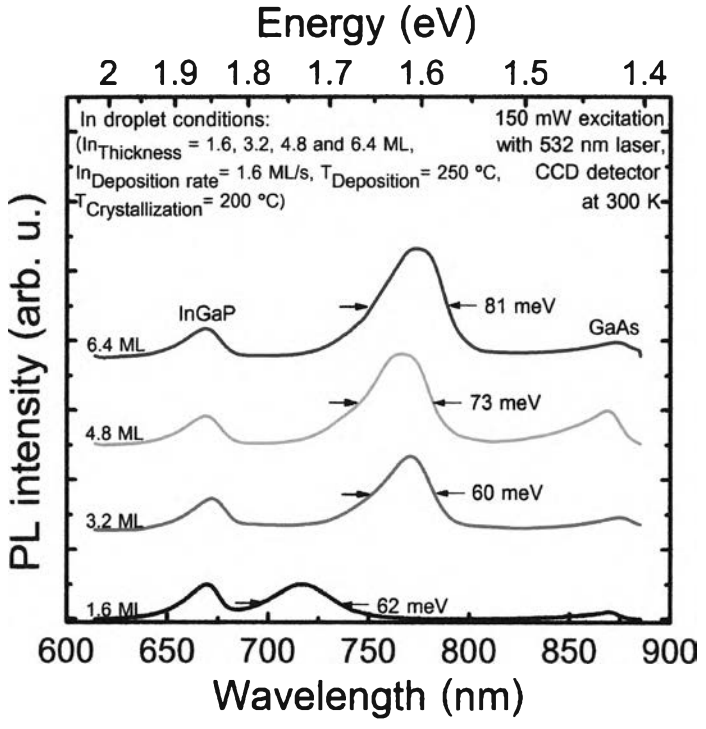

Figure 4.30 PL spectra of InP QRs and ring-shaped QDMs with various indium thickness measured by the micro-PL system at room temperature.

In view points of physical and optical properties of InP ring-shaped QDMs, the growth parameters have already been investigated and optimized. However, for some applications including quantum information processing (extended quantum cellular automata), the uniformity of ring-shaped QDMs, directional arrangement of QDs in ring-shaped QDMs and QD spacing in a QDM are critical parameters which the further investigation is mandatory. One of promising improvement method is to consider the growth parameters concurrently. This is because the growth parameters are not independently affects the QD and ring-shaped QDMs formation which is mainly determined by the volume of initial droplet. The other growth parameters, for example, P_2 BEP, crystallization time, should also been taken into consideration.

4.8 Power Dependence Photoluminescence of InP Ring-shaped Quantum Dot Molecules

In order to intensively understand about the optical properties of the InP ring-shaped QDMs, the power dependence photoluminescence of QDs are conducted by

macro-PL at 20 K. The investigated InP ring-shaped QDMs was fabricated using the deposition temperature of 250 °C, the crystallization temperature of 200 °C, the In deposition rate of 1.6 ML/s and the In thickness of 3.2 ML. The PL peak intensity dependence on the excitation power is illustrated in figure 4.31. The peak emissions of $In_{0.5}Ga_{0.5}P$, ground-state of InP ring-shaped QDMs and GaAs with 20 mW excitation power exist at 1.93 eV, 1.68 eV and 1.51 eV, respectively. With stronger applied excitation power, these PL peak intensities increase and the ground-state peaks of InP ring-shaped QDMs tend to the higher energy states (a little bit blueshift) and the first excited-state peak emerges and slightly grows. These results are explained by the tunnel coupling of QD and the state filling effect. According to Lippen (2006), the asymmetric broadening together with the shift of the PL peak towards higher energies are first indications for the formation of extended electron states in the QDMs due to tunnel coupling. Tunnel coupling of the QD ground states creates extended states with a distinct energy separation determined by the coupling strength. State filling with increase of the

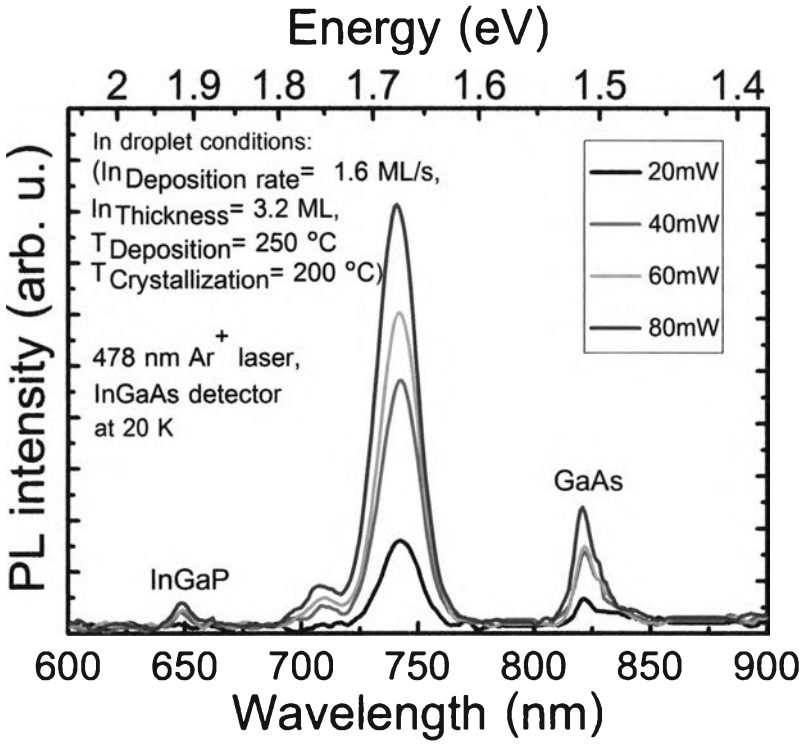

Figure 4.31 Power dependent PL spectra of InP ring-shaped QDMs which have the deposition temperature of 250 °C, the crystallization temperature of 200 °C, the In deposition rate of 1.6 ML/s and the In deposition rate of 3.2 ML.

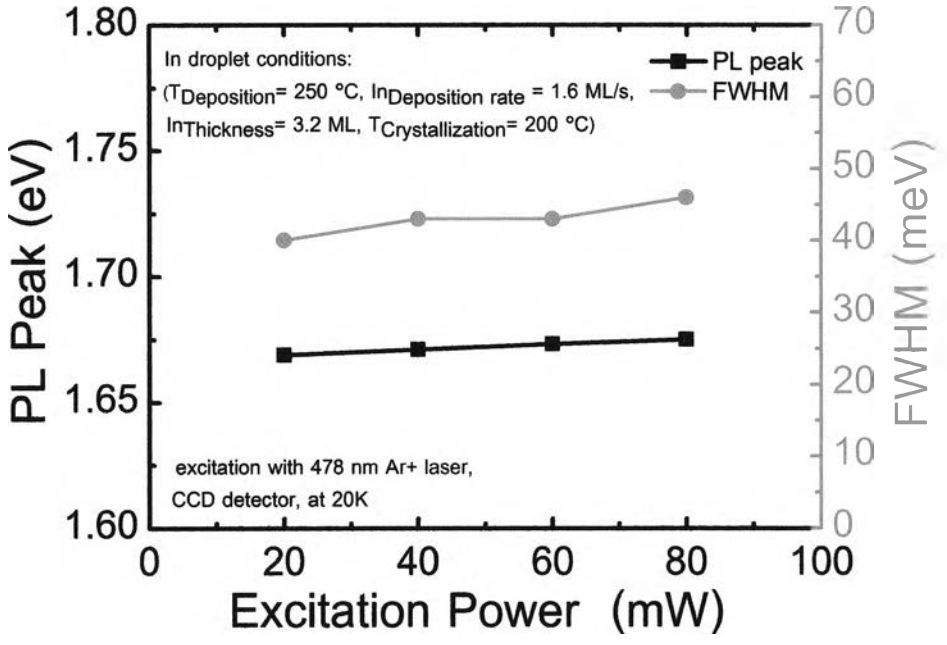

Figure 4.32 The relationship between excitation powers, FWHMs and peak emission positions.

excitation power accounts for the asymmetric broadening of the PL spectrum with unchanged low energy side. At much higher excitation power, the ground states of QD are almost fulfilled and the probability of radiative recombination of electrons in higher excited-states is increased. Therefore, the first excited-state peak appears at higher excitation power in this experiment. The tendencies of PL peak and FWHM of InP ring-shaped QDMs are shown in figure 4.32.

4.9 Temperature Dependence Photoluminescence of InP Ring-shaped Quantum Dot Molecules

The dependence of PL ground-state peak energies as a function of temperature for the InP ring-shaped QDMs is shown and compared with the temperature dependence of the bulk $In_{0.5}Ga_{0.5}P$ and GaAs bandgap in figure 4.33. The studied structure was fabricated with the deposition temperature of 250 °C, the crystallization temperature of 200 °C, the In deposition rate of 1.6 ML/s and the In thickness of 3.2 ML. The tendencies of PL peak and FWHM on the temperature are shown in figure 4.34. When the measuring temperature is increased from 20 K to 100 K, the redshifts of the relevant PL peak

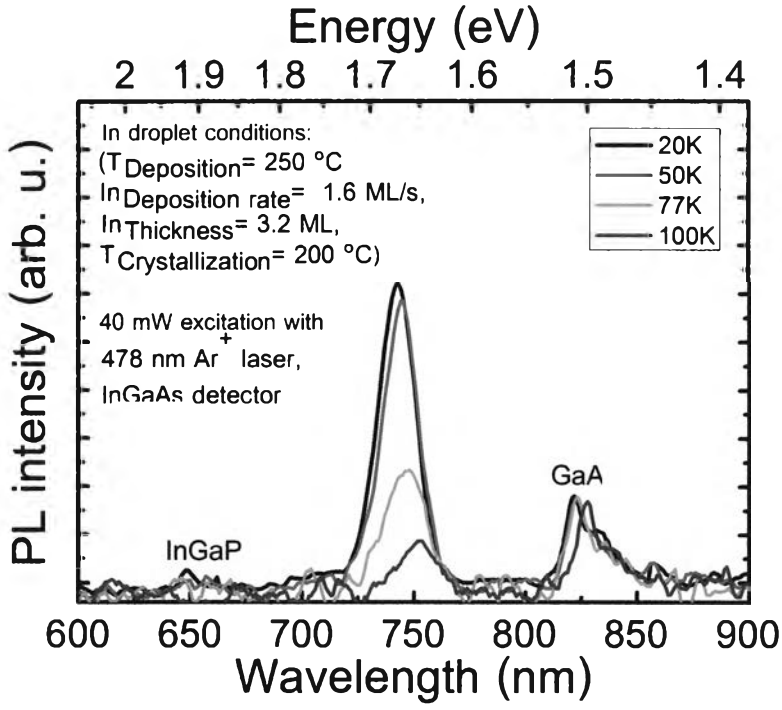

Figure 4.33 Temperature dependent PL spectra of InP ring-shaped QDMs which have the deposition temperature of 250 °C, the crystallization temperature of 200 °C, the In deposition rate of 1.6 ML/s and the In deposition rate of 3.2 ML.

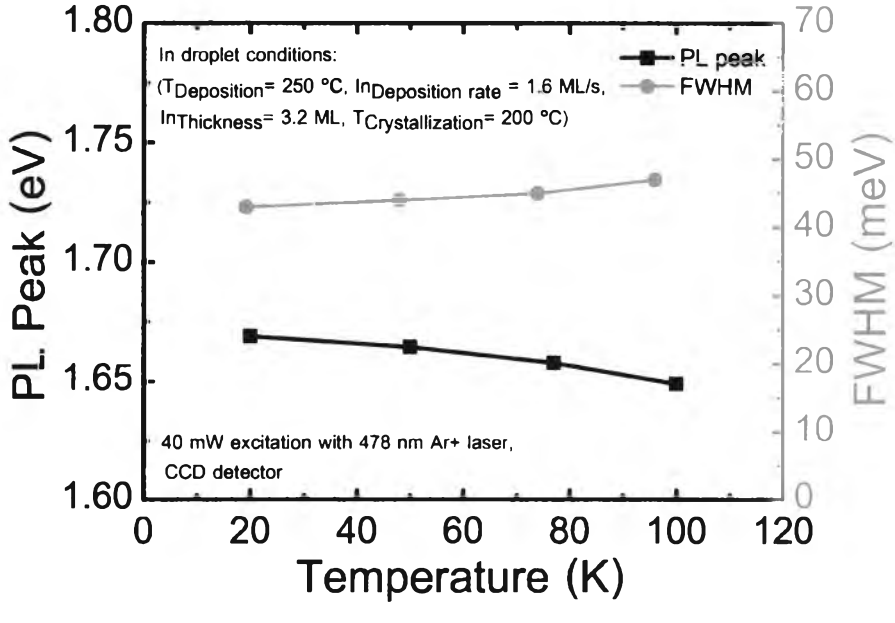

Figure 4.34 The relationship between temperatures, FWHMs and peak emission positions.

energies can be observed. The tendency of the PL peak intensities is lowered and the FWHM is increased with higher temperature. The main reason for these effects are the enhancement of the non-radiative recombination process by the increasing of electron-phonon interaction (scattering), the thermal distribution and the reduction of the excitonic temperature with increasing temperature (Lippen, 2006; Favero, 2003) and the high defects of the $In_{0.5}Ga_{0.5}P$ capping barrier (first capping with MEE). As a result, the photogenerated carriers escape from QDs into $In_{0.5}Ga_{0.5}P$ capping barriers and relax into the energetically lower energy state and recombine there or are trapped by the trapped level of $In_{0.5}Ga_{0.5}P$ capping barriers. Consequently, the PL peak is shifted to a lower energy level and the linewidth is increased and the integrated PL intensity reduces.

4.10 Characterization of InP Ring-shaped Quantum Dot Molecules by Transmission Electron Microscopy

Figure 4.35 (a) shows a schematic of sample structure that is used to measure TEM. Figure 4.35 (b) shows an overview cross-sectional TEM micrograph with magnification of 10,000 at 200 kV of InP ring-shaped QDM sample with the deposition temperature of 250 °C, the crystallization temperature of 200 °C, the indium deposition rate of 1.6 ML/s and the indium thickness of 3.2 ML. It demonstrates that the structure was grown without creating any dislocations or extended defects. The InP ring-shaped QDM layer embedded in $In_{0.5}Ga_{0.5}P$ matrices is clearly observed. The contrast of InP ring- shaped QDMs against $In_{0.5}Ga_{0.5}P$ is due to the difference in chemical composition and strain fields. Figure 4.35 (c) shows cross-sectional TEM micrograph with magnification of 50,000 at 200 kV of InP ring-shaped QDM on sample surface. The InP ring-shaped QDM appears mostly as dark disk that has two lobes corresponding to a cutting position trough the ring. The same contrast of InP ring-shaped QDMs indicate that the initial In droplets are completely formed to InP ring-shaped QDMs. The InP ring-shaped QDMs on the sample surface can be observed better than in the $In_{0.5}Ga_{0.5}P$ matrices due to no effect of thermal annealing during the capping process. The temperature changes the shape pf QD to a smaller one because of the interdiffusion between InP ring-shaped QDMs and $In_{0.5}Ga_{0.5}P$ (Jin-Phillipp et al., 2004). As a result, QDs in the $In_{0.5}Ga_{0.5}P$ matrices are unclearly observed in the cross-sectional TEM image.

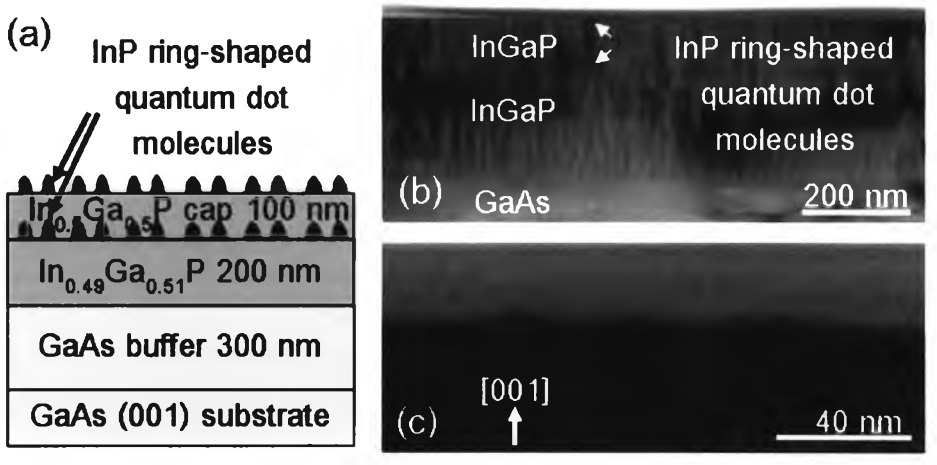

Figure 4.35 (a) Schematic of sample structure for TEM measurement, (b) Overview cross-sectional TEM micrograph of InP ring-shaped QDM sample with the deposition temperature of 250 °C, the crystallization temperature of 200 °C, the indium deposition rate of 1.6 ML/s and the indium deposition rate of 3.2 ML and (c) Cross-sectional TEM micrograph of the upper InP ring-shaped QDMs layer.